TWO-DIMENSIONAL CONDUCTIVITY AT $LaAlO_3/SrTiO_3$ INTERFACES

A Thesis Submitted to the Committee on Graduate Studies

in Partial Fulfillment of the Requirements for the

Degree of Master of Science in the Faculty of Art and Science

Trent University

Peterborough, Ontario, Canada

Materials Science M.Sc. Graduate Program

May 2014

Abstract

TWO-DIMENSIONAL CONDUCTIVITY AT $LaAlO_3/SrTiO_3$ **INTERFACES**

Amany Raslan

Experiments have observed a two-dimensional electron gas at the interface of two insulating oxides: strontium titanate ($SrTiO_3$) and lanthanum aluminate ($LaAlO_3$). These interfaces exhibit metallic, superconducting, and magnetic behaviours, which are strongly affected by impurities. Motivated by experiments, we introduce a simple model in which impurities lie at the interface. We treat the $LaAlO_3$ as an insulator and model the $SrTiO_3$ film. By solving a set of self-consistent Hartree equations for the charge density, we obtain the band structure of the $SrTiO_3$ film. We then study the relative contributions made by the occupied bands to the two-dimensional conductivity of the $LaAlO_3/SrTiO_3$ interface. We find that the fractional conductivity of each band depends on several parameters: the mass anisotropy, the filling, and the impurity potential.

Keywords: Two-dimensional electron gases, insulating oxides, impurities, conductivity.

Acknowledgements

I kneel humbly to **ALLAH** thanking **HIM** for showing me the right path, without **HIS** help my efforts would have gone astray.

My sincere thanks are directed to Prof. Bill Atkinson for his supervision, advice, encouragement, patient and persistent motivation to complete this work.

I would like to express the deepest appreciation to my committee members, Prof. Rachel Wortis, and Prof. Franco Gaspari for many interesting discussions we had in committee meetings.

I would like to extend my gratitude to the Physics and Astronomy Department staff, Trent University, for their kind support and help, and especially my officemate, Mr. Sinan Bulut.

Finally, I would like to thank my family for their encouragement and prayer, especially my parents, Khalil and Fatima. A very special thanks goes out to my sons, Ahmed and Ali, and my husband, Dr. Maher Ahmed, for their constant love and support.

Contents

List of Figures

List of Tables

Chapter 1

Introduction

Throughout human history on earth, human development was related to our understanding of the materials around us. This understanding appeared in the development of tools through the Stone, Bronze and Iron Ages. Ultimately, the electron's discovery and the development of quantum mechanics permitted the understanding of the electronic structure of materials, whose manipulation brought us to the silicon age. Silicon technology has grown very fast, and has improved the shape of our world. One goal of modern research is to find new materials with different functionalities than semiconductors. Recent attention has focused on transition metal oxides because they have strongly correlated electrons, and therefore have a greater variety of functionalities than conventional semiconductors. Examples of these functionalities include high-temperature superconductivity in $YBa_2Cu_3O_7$, a metal-insulator transition in VO_2, and magnetism in MnO.

Interfaces and surfaces are considered birthplaces for new and interesting phenomena because there may be structural, electronic, spin, and orbital reconstructions due to broken symmetries associated with the interface [1]. These reconstructions produce many fascinating physical properties, for example the two-dimensional electron gas that forms at semiconductor interfaces, and which is key to devices like transistors, lasers or solar cells [2]. For that reason, it was expected that oxide interfaces will provide new and interesting phenomena, especially for oxides whose bulk phases already have interesting functionalities. Historically, this research was limited by difficulties in growing epitaxial oxide heterostructures. Recently, these difficulties were overcome after the development of new deposition techniques like molecular beam epitaxy and pulsed laser deposition. Thus, it is becoming possible to grow high-quality oxide heterostructures with atomically sharp interfaces [3].

In 2004, Ohtomo and Hwang grew heterointerfaces between two insulating oxide materials, strontium titanate ($SrTiO_3$) and lanthanum aluminate ($LaAlO_3$), by using

the pulsed laser deposition method. Surprisingly, they observed a high-mobility two-dimensional electron gas at the interface [4]. Since then, this amazing property has attracted worldwide attention, and is confirmed experimentally by many studies [5–11]. Two-dimensional electron gases (2DEG) have been formed at different oxide interfaces, including $LaTiO_3/SrTiO_3$ [12], $LaVO_3/SrTiO_3$ [13], $LaGaO_3/SrTiO_3$ [14], and $KTaO_3/SrTiO_3$ [15] interfaces. It is found that, at the interface, the 2DEG has a mobility, up to $10^4 cm^2/Vs$ [4], a density of nearly $10^{14}/cm^2$ and a short confinement length $\approx 7nm$ [16, 17]. These interesting properties make $2DEG$ at oxide interfaces a new candidate for future technology.

1.1 $LaAlO_3/SrTiO_3$ Interface

Our concern in this dissertation is the interface between $SrTiO_3$ and $LaAlO_3$. $SrTiO_3$ is a perovskite oxide material whose structure is shown in Fig. 1.1. It has a lattice constant ($3.905\mathring{A}$) near to many other oxides, and it is chemically inert and does not interact with the deposited materials. These properties allow for epitaxial growth of oxides on $SrTiO_3$ substrates. For that reason, $SrTiO_3$ is known as a workhorse oxide [18]. Electronically, $SrTiO_3$ is an insulator with a wide band gap of $\approx 3.25eV$. However, it can be made conducting by introducing oxygen vacancies during synthesis or by doping with elements like La. $LaAlO_3$ is a band insulator with a wide band gap of $\approx 5.6eV$. It has a perovskite structure, and has a lattice constant of $3.791\mathring{A}$. There is a lattice mismatch of $\approx 3\%$ with $SrTiO_3$, which allows the epitaxial growth of $LaAlO_3$ on $SrTiO_3$ to obtain high-quality $LaAlO_3/SrTiO_3$ heterostructures [4].

Ohtomo and Hwang [4] observed that to get a conducting $LaAlO_3/SrTiO_3$ interface, the interface has to be between LaO and TiO_2 layers, which is called an n-type interface because it is doped by electrons. Conversely, if the interface is between AlO_2

and SrO layers, the $LaAlO_3/SrTiO_3$ interface is *p*-type because it is doped by holes. However, unlike the *n*-type interface, it is found to be insulating [4]. Hence, most work has focused on growing $LaAlO_3$ on TiO_2-terminated $SrTiO_3$ substrates.

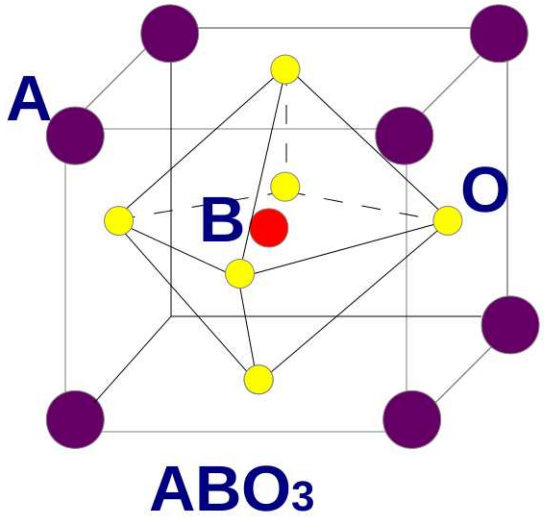

Figure 1.1: The perovskite unit cell for ABO_3. A, B are cations and O is Oxygen.

The $LaAlO_3/SrTiO_3$ interface is considered to be the most interesting epitaxial oxide heterostructure. S. Thiel et al. [6] observed a large electric-field response of the 2DEG, which can be tuned from an insulating to a metallic state. In addition, [19] and [20] report a transition to a two-dimensional superconducting state at a temperature $\approx 200mK$. Moreover, even though bulk $LaAlO_3$ and $SrTiO_3$ are nonmagnetic materials, a magnetic ordering is induced at the $LaAlO_3/SrTiO_3$ interface [21]. These properties suggest that $LaAlO_3/SrTiO_3$ interfaces may be useful as field-effect [22] or spintronic devices [23].

1.1.1 Origin of the 2DEG at the $LaAlO_3/SrTiO_3$ interface

The most challenging question which is not fully answered yet is what is the origin of the 2DEG at the oxide interfaces? Indeed, there are a lot of experimental and theoretical studies which try to answer that question, but there is still no unified mechanism for the doping at the oxide interfaces. Depending on the growth conditions, there are three main mechanisms which have been proposed in these studies for the source of the 2DEG: the polar nature of the $LaAlO_3$ atomic planes (polar discontinuity), oxygen vacancies, and cation intermixing.

Polar Discontinuity

As mentioned before, $LaAlO_3$ and $SrTiO_3$ have perovskite structures, shown in Fig. 1.1. In the (001) direction, the ABO_3 perovskite structure consists of layers of AO and BO_2 planes. To keep ABO_3 neutral, the cations A and B may have formal valence $A^{+2}B^{+4}$, $A^{+4}B^{+2}$ or $A^{+3}B^{+3}$, because oxygen has a formal valence of O^{-2}. In $LaAlO_3/SrTiO_3$ heterostructures, the cation valences are Sr^{+2}, Ti^{+4}, La^{+3} and Al^{+3}. Accordingly, $SrTiO_3$ ($A^{+2}B^{+4}O_3^{-6}$) is stacked in alternating layers of $Sr^{+2}O^{-2}$(AO) and $Ti^{+4}O_2^{-4}$(BO_2), which are neutral planes, having no net charges. On the other hand, $LaAlO_3$($A^{+3}B^{+3}O_3^{-6}$) has planes of $La^{+3}O^{-2}$(AO) and $Al^{+3}O_2^{-4}$(BO_2), with net charge $+1$ and -1, respectively. Thus, the interface of $LaAlO_3$ and $SrTiO_3$ is between polar $LaAlO_3$ and non-polar $SrTiO_3$ materials, leading to a polar discontinuity at the interface. If we imagine $LaAlO_3$ as a chain of capacitors in series, then a potential will grow through each capacitor leading to a polar catastrophe, as illustrated in Fig. 1.2. The polar catastrophe was observed previously in conventional semiconductors when a polar film, GaAs, was deposited on a non-polar material, Ge or Si. In this case, an atomic reconstruction occurred, which eliminated the potential divergence [24, 25].

Nakagawa et al. proposed that "If the electrons can move, the atoms do not have to" [18]. The existence of Ti at the interface gives the possibility of an electronic reconstruction because Ti has a multivalent nature, Ti^{+3} or Ti^{+4}. Accordingly, if a half-electron per unit cell is transferred from the top layer of the $LaAlO_3$ to the interface, it will find accommodation in a Ti atom at the interface, which will become $Ti^{+3.5}$, as shown in Fig. 1.2. This electronic reconstruction compensates the electric field in the $LaAlO_3$ layers (Fig. 1.2), and solves the polar catastrophe problem.

Ohtomo and Hwang [4] explained their discovery of the 2DEG at the $LaAlO_3/SrTiO_3$ interface by proposing the polar discontinuity scenario. They proposed that the *n*-type interface is conducting because it is possible to form $Ti^{+3.5}$. However, in case of the *p*-type interface, the electronic reconstruction occurs by transferring a half-hole from the $LaAlO_3$ surface layer. Since there is no possibility to form $Ti^{+4.5}$, the holes are trapped by oxygen vacancies at the interface, which leads the *p*-interface to be insulating. The polar catastrophe scenario was supported experimentally by Thiel et al. [6], who found that there is a minimum $LaAlO_3$ thickness, beyond which the $LaAlO_3/SrTiO_3$ interface is conducting. This means that, when the thickness of $LaAlO_3$ layers is small, the potential difference between $LaAlO_3$ surface and the interface is small. Once the $LaAlO_3$ thickness exceeds a critical value, ≈ 4 unit cells [6], the potential becomes larger than the $LaAlO_3$ band gap. As a result, charges are transferred to the interface. However, the measured 2DEG density is much smaller ($\lesssim 1.8\text{x}10^{14} cm^{-2}$) than is expected from the electronic reconstruction scenario ($\approx 3.3\text{x}10^{14} cm^{-2}$). This raises doubts that the polar discontinuity is the only mechanism for the 2DEG formation at the $LaAlO_3/SrTiO_3$ interfaces.

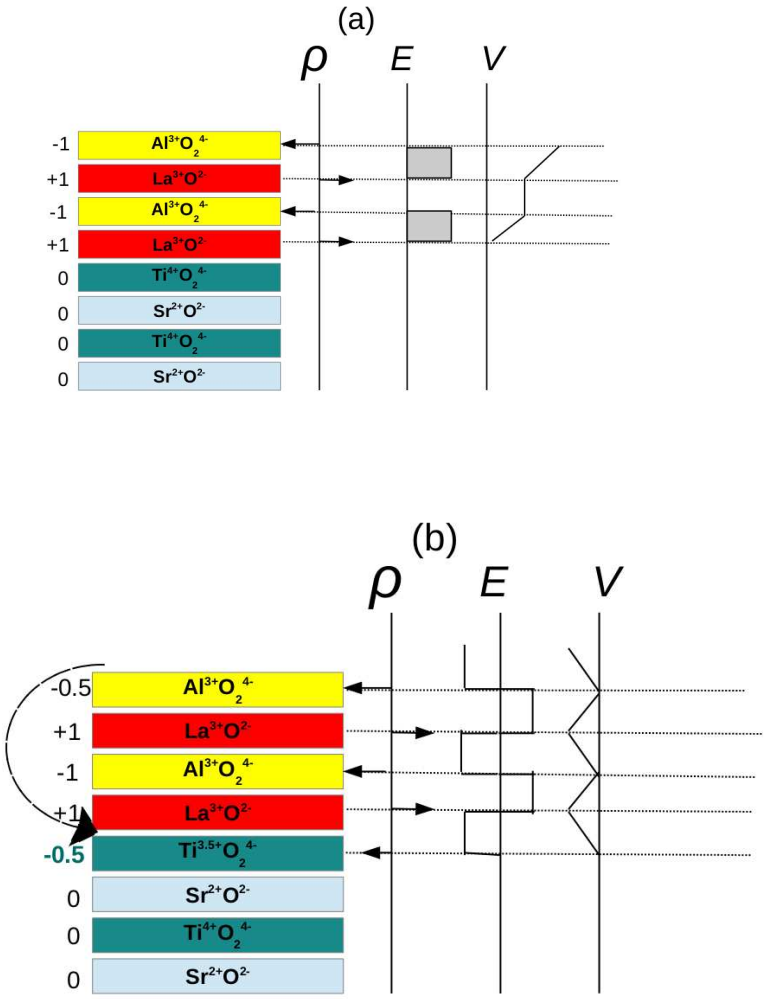

Figure 1.2: (a) A schematic picture of how the polar catastrophe occurs in the $LaAlO_3/SrTiO_3$ structure, and (b) a schematic picture showing the electronic reconstruction at the $LaAlO_3/SrTiO_3$ interface. ρ is the net charge density for each layer, and the arrows show the ρ's magnitude and sign. E is the electric field and V is the potential inside the $LaAlO_3$ layers.

Oxygen Vacancies

Oxygen vacancies are a common type of defect in oxide materials, which are created during sample growth, especially at low oxygen pressure, and act as electron donors. Thus, they are proposed as a source of the 2DEG at the $LaAlO_3/SrTiO_3$ interface. Extensive studies have explored oxygen vacancies in $LaAlO_3/SrTiO_3$ heterostructure systems: some of them have shown that oxygen vacancies contribute to the 2DEG [8, 26, 27], while others suggest that magnetic ordering at the interface is due to oxygen vacancies [28–30]. On the other hand, some studies point out that the oxygen vacancies alone can't explain why the conducting interface is formed only after a critical $LaAlO_3$ thickness [31]. In conclusion, these studies can't affirm that the oxygen vacancies alone can explain the origin of the 2DEG but suggest that they may play a role.

Cation intermixing

Cation intermixing at the the $LaAlO_3/SrTiO_3$ interface was first observed by Nakagawa et al. [18]. It occurs through redistribution of the Sr^{+2} and La^{+3} at the interface, which dopes the interface. Cation intermixing also disorders the interface layers. By using atomic-resolution electron energy loss spectroscopy, Nakagawa et al. found that the roughness of the n-type interface (1.9 unit cells) is larger than the roughness of p-type interface (0.77 unit cells). This means more cation intermixing at the n-type interface than the p-type interface. For that reason, the authors argued that the n-type interface is more doped than the p-type, and that explains why the n-type interface is conducting and the p-type is insulating. Later work confirmed that cation intermixing is one source of the 2DEG [32–38].

In summary, the doping sources of the 2DEG at the $LaAlO_3/SrTiO_3$ interface essentially depend on the growth conditions. Three mechanisms, electronic reconstruc-

tion, oxygen vacancies, and cation intermixing, together contribute to the 2DEG formation. In fact, it was found that samples which are grown under low oxygen pressure ($\lesssim 10^6$mbar) have oxygen vacancies as the dominant mechanism for the conductivity, while samples which are grown under higher oxygen pressure ($\gtrsim 10^5$mbar) have the polar discontinuity as the dominant mechanism.

1.2 Conductivity at the $LaAlO_3/SrTiO_3$ interface

From our previous discussion, we conclude that the conductivity of the $LaAlO_3/SrTiO_3$ interfaces depends on the substrate termination [4], the $LaAlO_3$ thickness [6], and impurities and defects [39]. As is known, impurities play a crucial role in understating and controlling the conductivity of $LaAlO_3/SrTiO_3$ interfaces. These impurities can be oxygen vacancies that are created during the growth processing, or dislocations due to cation intermixing or lattice distortion at the interface [18,38]. Their effect on the electronic and magnetic properties of the $LaAlO_3/SrTiO_3$ hetetrostructres has been explored by many experimental and theoretical studies. The results of these studies depends strongly on the position of the impurities in the heterostructures. For example, it is predicted that oxygen vacancies at the $LaAlO_3$ surface [40–42] are an important source of the 2DEG at the interface. Oxygen vacancies at the $LaAlO_3/SrTiO_3$ interfaces can also increase the density and mobility of the 2DEG [15]. Other kinds of impurities may trap or scatter the carriers and lead to a lower 2DEG mobility [18,38]. Oxygen vacancies in the $SrTiO_3$ bulk create a three-dimensional gas in $SrTiO_3$ substrate [40].

Experimental studies [43, 44] that give evidence for the existence of impurities at the interface motivated us to introduce a simple model to study the interface conductivity. Our model assumes that the impurities lie in the TiO_2 layer adjacent to the

interface. The impurity density is assumed low, so we can use a dilute approximation, and we focus on n-type interfaces. Then, the goal of this thesis is to calculate the contributions of occupied bands to the total interface conductivity.

1.3 Thesis Outline

The goal of this thesis is to study the two-dimensional conductivity at $LaAlO_3/SrTiO_3$ interfaces. In chapter 2, we will introduce a simple model to study the contributions of occupied bands to the 2D conductivity. This will done in two steps: first we will write the tight-binding model to describe the $SrTiO_3$ band Structure, and then develop the model for impurities to study the interface conductivity. In chapter 3, we will explore and analyze model results in detail. Finally, in chapter 4, we will provide conclusions about our calculations.

Chapter 2

Theoretical Model

2.1 Introduction

In this chapter, we introduce our simple model for the $LaAlO_3/SrTiO_3$ interface. The goal of the model is to describe the effect of impurities on the $LaAlO_3/SrTiO_3$ interface by calculating the contribution of partially filled bands to the conductivity. This leads us later to compare our model to experimental data. The model is built on the following assumptions:

- Because $LaAlO_3$ has a wider band gap than $SrTiO_3$ (5.6eV and 3.3eV respectively), see Fig. 2.1, the two-dimensional electron gas energetically prefers to occupy the $SrTiO_3$ conduction band than the $LaAlO_3$ conduction band. Thus, we treat the $LaAlO_3$ as an insulator and don't include any orbitals from it in our model.

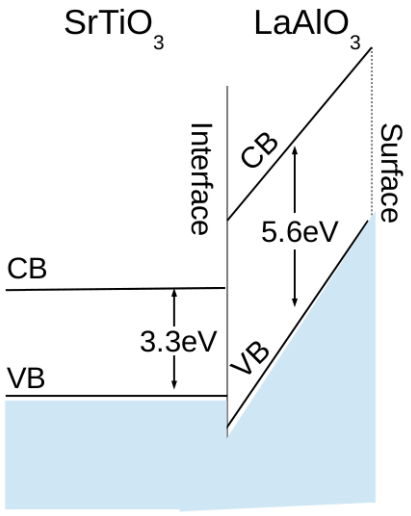

Figure 2.1: Sketch of $LaAlO_3$ and $SrTiO_3$ band gaps. CB denotes the conduction band and VB denotes valence band.

- The $SrTiO_3$ band gap is between an O2p orbital valence band and a Ti t_{2g} conduction band [45]. Thus, we exclude O atoms and model only Ti t_{2g} orbitals using the tight-binding model.

- We assume that there are three t_{2g} orbitals per unit cell, d_{xy}, d_{xz} and d_{yz}, as shown in Fig. 2.2.

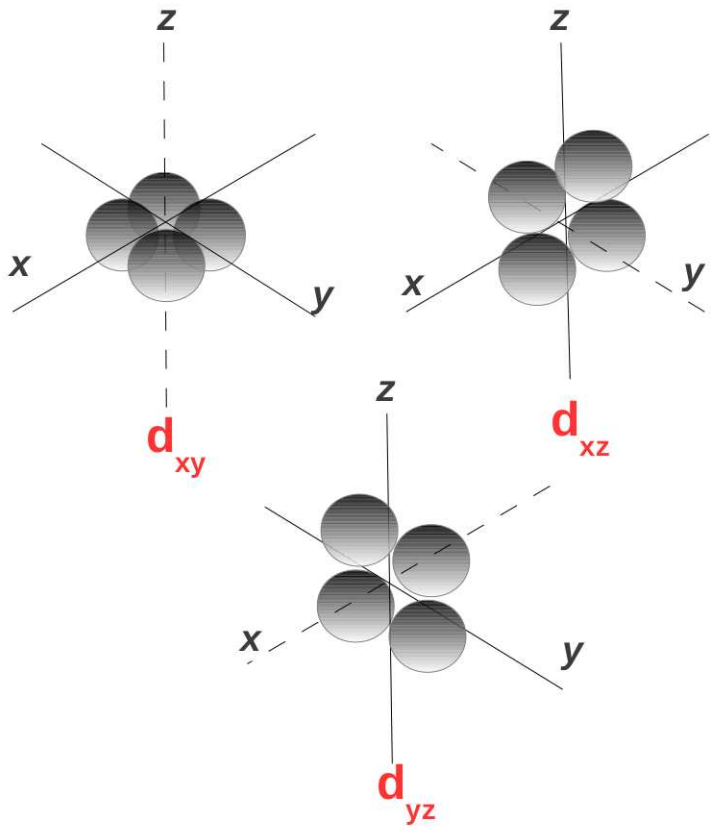

Figure 2.2: Schematic representation of the Ti t_{2g} orbitals, d_{xy}, d_{xz} and d_{yz}.

We begin by calculating the band structure of bulk $SrTiO_3$, which is included as a simple case to help understand the more complicated $LaAlO_3/SrTiO_3$ interface. Then we build the Hamiltonian of the $LaAlO_3/SrTiO_3$ interface and finally include impurities at the interface.

2.2 Theoretical Model

2.2.1 Bulk $SrTiO_3$

To introduce the model, we begin with the simplest case in which we impose periodic boundary conditions in the x, y and z directions. The noninteracting Hamiltonian for $SrTiO_3$ is

$$\hat{H}_{3D} = \sum_{ij} \sum_{\alpha,\beta} \sum_{\sigma} c^{\dagger}_{i\alpha\sigma} t_{i\alpha,j\beta} c_{j\beta\sigma} \tag{2.1}$$

where

- $c_{j\beta\sigma}$ is the annihilation operator for an electron with spin σ in unit cell j in orbital type α.
- $c^{\dagger}_{i\alpha\sigma}$ is the corresponding creation operator.
- $t_{i\alpha,j\beta}$ is the hopping matrix element of the periodic crystal Hamiltonian $H = \frac{-\hbar^2}{2m}\nabla^2 + V(\mathbf{r})$ between orbital α in unit cell i and orbital β in unit cell j,

$$t_{i\alpha,j\beta} = \langle i\alpha | H | j\beta \rangle. \tag{2.2}$$

- $\alpha = 1, 2$ and 3 for d_{xy}, d_{xz} and d_{yz} orbitals, respectively.

We diagonalize the Hamiltonian by Fourier transforming in all three dimensions (x,y and z) to go to k-space. Explicitly, we can define

$$c_{j\beta\sigma} = \frac{1}{\sqrt{N_k}} \sum_{\mathbf{k}} e^{i\mathbf{k}\cdot\mathbf{r}_{j\beta}} c_{\mathbf{k}\beta\sigma} \tag{2.3}$$

$$c^{\dagger}_{i\alpha\sigma} = \frac{1}{\sqrt{N_k}} \sum_{\mathbf{k}'} e^{-i\mathbf{k}'\cdot\mathbf{r}_{i\alpha}} c^{\dagger}_{\mathbf{k}'\alpha\sigma} \tag{2.4}$$

where

- $\mathbf{k} = (k_x, k_y, k_z)$ is the k-space coordinate,

- $\mathbf{r}_{i\alpha} = (x_{i\alpha}, y_{i\alpha}, z_{i\alpha})$ is a 3-dimensional position vector of orbital α in the i^{th} unit cell. Because we include only the Ti t_{2g} orbitals, the $\mathbf{r}_{i\alpha}$ is independent of α in our model.

- N_k is the number of unit cells.

Then we substitute Eq. (2.3) and (2.4) into Eq.(2.1) to obtain,

$$\hat{H}_{3D} = \frac{1}{N_k} \sum_{ij} \sum_{\alpha,\beta} \sum_{\sigma} \sum_{\mathbf{k}} \sum_{\mathbf{k}'} e^{-i\mathbf{k}'\cdot\mathbf{r}_{i\alpha}} c^{\dagger}_{\mathbf{k}'\alpha\sigma} t_{i\alpha,j\beta} e^{i\mathbf{k}\cdot\mathbf{r}_{j\beta}} c_{\mathbf{k}\beta\sigma}. \tag{2.5}$$

According to experiments [46] and density-functional theory calculations [47–49], the hopping elements between different orbital types are very small compared to the hopping between the same orbital types. Thus we consider only hopping $t_{i\alpha,j\alpha}$ between the same orbital types. Also, according to the tight-binding assumption, we consider nearest-neighbor hopping only. This leads us to define $\mathbf{d}$ such that

$$\mathbf{r}_{j\alpha} = \mathbf{r}_{i\alpha} + \mathbf{d} \tag{2.6}$$

where $\mathbf{d}$ is a lattice vector connecting nearest neighbor unit cells. Then, we use the fact that $t_{i\alpha,j\alpha}$ only depends on the displacement $\mathbf{d}$ between orbitals

$$t_{i\alpha,j\alpha} = t(\mathbf{r}_{i\alpha} - \mathbf{r}_{j\alpha}) = t(\mathbf{r}_{i\alpha} - \mathbf{r}_{i\alpha} - \mathbf{d}) = t_{\alpha,\alpha}(-\mathbf{d}) = t_{\alpha,\alpha}(\mathbf{d}), \tag{2.7}$$

so that

$$\hat{H}_{3D} = \frac{1}{N_k} \sum_{i} \sum_{\mathbf{d}} \sum_{\alpha} \sum_{\sigma} \sum_{\mathbf{k}} \sum_{\mathbf{k}'} e^{i(\mathbf{k}-\mathbf{k}')\cdot\mathbf{r}_{i\alpha}} c^{\dagger}_{\mathbf{k}'\alpha\sigma} t_{\alpha,\alpha}(\mathbf{d}) e^{i\mathbf{k}\cdot\mathbf{d}} c_{\mathbf{k}\alpha\sigma}. \tag{2.8}$$

Since

$$\frac{1}{N_k} \sum_{i} e^{i(\mathbf{k}-\mathbf{k}')\cdot\mathbf{r}_{i\alpha}} = \delta_{\mathbf{k},\mathbf{k}'}, \tag{2.9}$$

then

$$\hat{H}_{3D} = \sum_{\mathbf{d}} \sum_{\alpha} \sum_{\sigma} \sum_{\mathbf{k}} c^{\dagger}_{\mathbf{k}\alpha\sigma} t_{\alpha,\alpha}(\mathbf{d}) e^{i\mathbf{k}\cdot\mathbf{d}} c_{\mathbf{k}\alpha\sigma}. \tag{2.10}$$

Then, we define

$$\epsilon_{\alpha}(\mathbf{k}) = \sum_{\mathbf{d}} t_{\alpha,\alpha}(\mathbf{d}) e^{i\mathbf{k}\cdot\mathbf{d}}. \tag{2.11}$$

Depending on the value of $\mathbf{d}$, $t_{\alpha,\alpha}(\mathbf{d})$ takes three different values:

- When $\mathbf{d} = \mathbf{0}$,

  $$t_{\alpha,\alpha}(0) = \epsilon_{t_{2g}},$$

  where $\epsilon_{t_{2g}}$ is the on-site orbital energy.

- When $\mathbf{d}$ is in the α-plane,

  $$t_{\alpha,\alpha}(\mathbf{d}) = t^{\parallel}_{\alpha},$$

  where $t^{\parallel}_{\alpha}$ is the hopping term in the α-plane between two d_{α} orbitals. For example, $t^{\parallel}_{xy}$ is the hopping term in the x-y plane between two d_{xy} orbitals, as shown in Fig. 2.3.

- When $\mathbf{d}$ is along an axis perpendicular to the α-plane,

  $$t_{\alpha,\alpha}(\mathbf{d}) = t^{\perp}_{\alpha},$$

  where $t^{\perp}_{\alpha}$ is the hopping term along the axis perpendicular to the α-plane between two d_{α} orbitals. For example, $t^{\perp}_{xy}$ is the hopping term along the z-axis between two d_{xy} orbitals, as shown in Fig. 2.3.

Therefore

$$\hat{H}_{3D} = \sum_{\mathbf{k}} \sum_{\sigma} \Psi^{\dagger}_{\mathbf{k}\sigma} h(\mathbf{k}) \Psi_{\mathbf{k}\sigma}, \tag{2.12}$$

with $\Psi^{\dagger}_{\mathbf{k}\sigma} = [c^{\dagger}_{\mathbf{k}(xy)\sigma}, c^{\dagger}_{\mathbf{k}(xz)\sigma}, c^{\dagger}_{\mathbf{k}(yz)\sigma}]$, and

$$h(\mathbf{k}) = \begin{bmatrix} \epsilon_{xy}(\mathbf{k}) & 0 & 0 \\ 0 & \epsilon_{xz}(\mathbf{k}) & 0 \\ 0 & 0 & \epsilon_{yz}(\mathbf{k}) \end{bmatrix},$$

with

$$\epsilon_{xy}(\mathbf{k}) = \epsilon_{t_{2g}} - 2t^{\parallel}_{xy}(\cos k_x a + \cos k_y a) - 2t^{\perp}_{xy} \cos k_z a, \tag{2.13}$$

$$\epsilon_{xz}(\mathbf{k}) = \epsilon_{t_{2g}} - 2t^{\parallel}_{xz}(\cos k_x a + \cos k_z a) - 2t^{\perp}_{xz} \cos k_y a, \tag{2.14}$$

$$\epsilon_{yz}(\mathbf{k}) = \epsilon_{t_{2g}} - 2t^{\parallel}_{yz}(\cos k_y a + \cos k_z a) - 2t^{\perp}_{yz} \cos k_x a. \tag{2.15}$$

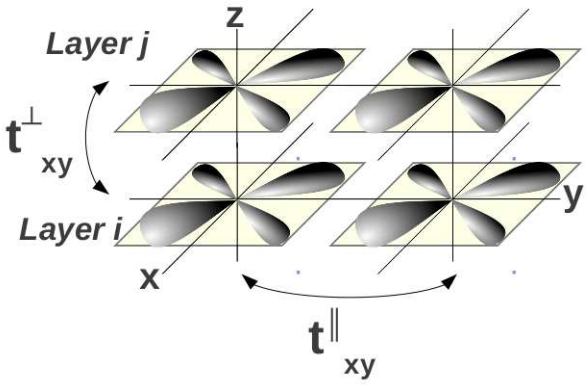

Figure 2.3: Schematic representation of the parallel and perpendicular hopping terms between d_{xy} orbitals.

Considering the symmetry of our system, we might expect that

$$t^{\parallel}_{xy} = t^{\parallel}_{xz} = t^{\parallel}_{yz} = t^{\parallel}, \tag{2.16}$$

and

$$t^{\perp}_{xy} = t^{\perp}_{xz} = t^{\perp}_{yz} = t^{\perp}. \tag{2.17}$$

As shown in Fig. 2.3, the d_{xy} orbital wave-function overlaps more in the x-y plane than along the z-axis, and thus we assume in our model that the hopping in any plane

(the parallel hopping) is greater than the hopping along the perpendicular axis (the perpendicular hopping), namely that $t^{\parallel} > t^{\perp}$ [49–51].

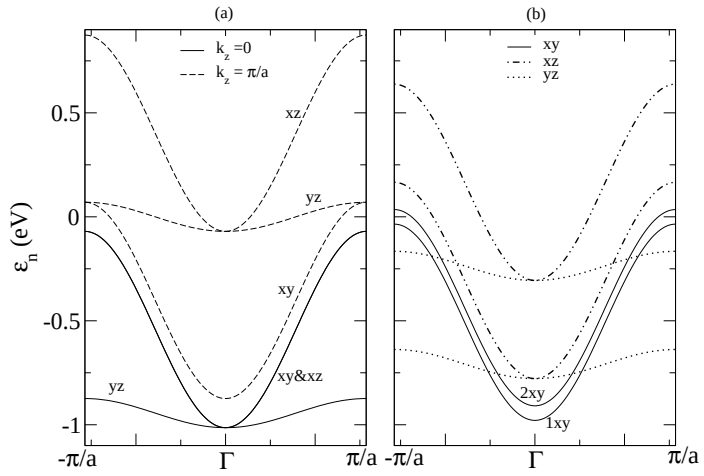

Figure 2.4: (a) The band structure of the bulk $SrTiO_3$ along the k_x-direction at two values of $k_z = 0$, and π/a, $k_y = 0$. (b) The band structure of a two layer $SrTiO_3$ film along the k_x-direction in the non-interacting case. In our calculations, $t^{\parallel} = 236$meV and $t^{\perp} = 35$meV [49].

We plot Eqs.(2.13), (2.14), and (2.15) along the k_x-axis at two k_z values, 0 and $\frac{\pi}{a}$, and $k_y = 0$ in Fig. 2.4(a). At $\mathbf{k} = \mathbf{0}$, the three bands, xy, xz and yz are degenerate because the three equations, Eqs. (2.13), (2.14), and (2.15), are equal at $k_x = k_y = k_z = 0$. Away from the Γ point, the yz band has a small dispersion $\approx 0.14eV$, and the xy and the xz bands are fully degenerate with each other, with a large dispersion $\approx 0.9eV$. These behaviours are because the band structure is plotted along the k_x direction and $t^{\parallel} > t^{\perp}$. This band structure shows a good agreement with previous calculations [45, 50, 51].

At $k_z = \pi/a$, the three bands are shifted from their values at $k_z = 0$, with a small shift for the xy band and a large shift for the xz and yz bands: the xy band is shifted by $2t^{\perp}$, and the xz and yz bands are shifted by $2t^{\parallel}$ as shown in Eqs. (2.13), (2.14), and (2.15). If we plot Eqs.(2.13), (2.14), and (2.15) along the k_y-axis and $k_x = 0$, the xz and yz bands will switch roles.

2.2.2 The $LaAlO_3/SrTiO_3$ Interface

The way we model the $LaAlO_3/SrTiO_3$ interface differs from the bulk case in that we assume that one surface of the $SrTiO_3$ thin film forms an interface with the $LaAlO_3$ film, as shown in Fig. 2.5. Figure 2.5 shows a sketch of the $LaAlO_3/SrTiO_3$ interface along with the electrostatic potentials generated by the surface and interface charges. To model this, we apply open boundary conditions along the z-axis.

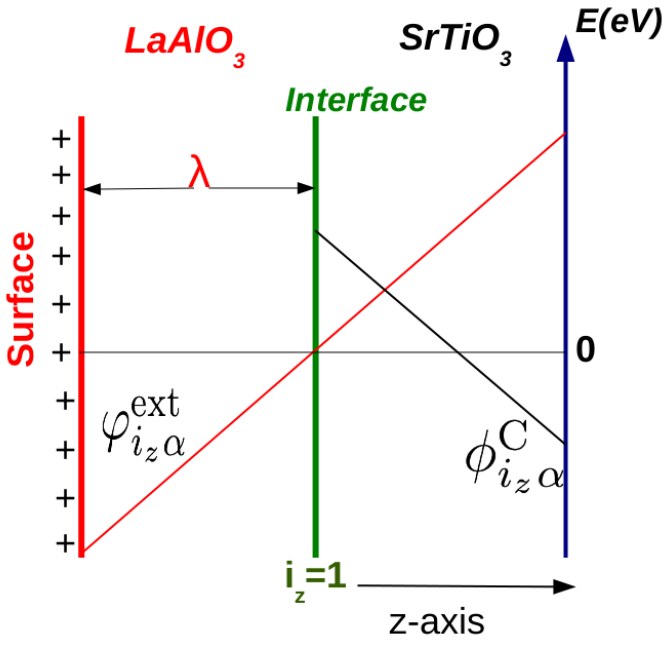

Figure 2.5: Sketch of the $LaAlO_3/SrTiO_3$ interface model. $\varphi^{\text{ext}}_{i_z\alpha}$ is the external potential energy due to charges at the $LaAlO_3$ surface, Eq. (2.39). $\phi^{\text{C}}_{i_z\alpha}$ is the Coulomb potential energy due to charges in the $SrTiO_3$ film, Eq. (2.52), λ is the $LaAlO_3$, and i_z is the $SrTiO_3$ layer index, where $i_z = 1$ indicates the $LaAlO_3/SrTiO_3$ interface.

The Hamiltonian for the $SrTiO_3$ thin film is

$$\hat{H} = \hat{H}_0 + \hat{V}_{ext} + \hat{V}_C, \tag{2.18}$$

where

- $\hat{H}_0$ is the noninteracting Hamiltonian.

- $\hat{V}_{ext}$ is the external potential energy in the $SrTiO_3$ thin film due to the charge at the $LaAlO_3$ surface, which comes from the electronic reconstruction (Fig. 2.5).
- $\hat{V}_C$ is the Coulomb interaction energy due to electrons in the $SrTiO_3$ thin film, (Fig. 2.5).

We begin with the simplest case, where there are no interactions in the $SrTiO_3$ film, to see the effect of the interface on the $SrTiO_3$ band structure. Then, we include the electron interactions and external potential.

Noninteracting Hamiltonian $\hat{H}_0$

The noninteracting Hamiltonian for the $SrTiO_3$ thin film is

$$\hat{H}_0 = \sum_{ij} \sum_{\alpha,\beta} \sum_{\sigma} c^{\dagger}_{i\alpha\sigma} t_{i\alpha,j\beta} c_{j\beta\sigma}, \tag{2.19}$$

where $t_{i\alpha,j\beta}$ is the same as in the bulk case, except that there is no hopping through the $LaAlO_3/SrTiO_3$ interface. Thus the hopping matrix elements through the top and bottom surfaces of the $SrTiO_3$ film are zero. We perform the Fourier transform in two dimensions (x and y), so we can define

$$c_{j\beta\sigma} = \frac{1}{\sqrt{N_{k_x k_y}}} \sum_{k_x k_y} e^{i\vec{k}\cdot\vec{r}_{j_x j_y \beta}} c_{j_z \vec{k} \beta\sigma}, \tag{2.20}$$

$$c^{\dagger}_{i\alpha\sigma} = \frac{1}{\sqrt{N_{k_x k_y}}} \sum_{k'_x k'_y} e^{-i\vec{k}'\cdot\vec{r}_{i_x i_y \alpha}} c_{i_z \vec{k}' \alpha\sigma}, \tag{2.21}$$

where

- $N_{k_x k_y}$ is the number of k_x and k_y points.
- $i = (i_x, i_y, i_z)$ and $j = (j_x, j_y, j_z)$ are unit cell indices.

- i_z indicates which layer the orbital is in, where the first layer ($i_z = 1$) is adjacent to the interface.
- $\vec{k}$ is a two dimensional vector (k_x, k_y).
- $\vec{r}_{i_x i_y \alpha}$ and $\vec{r}_{j_x j_y \beta}$ are two dimensional vectors, such that

$$\vec{r}_{i_x i_y \alpha} = a(x_{i\alpha}, y_{i\alpha}), \tag{2.22}$$

$$\vec{r}_{j_x j_y \beta} = a(x_{j\beta}, y_{j\beta}). \tag{2.23}$$

We substitute Eq. (2.20) and Eq. (2.21) into Eq. (2.19) to obtain

$$\hat{H}_0 = \frac{1}{N_{k_x k_y}} \sum_{ij} \sum_{\alpha,\beta} \sum_{\sigma} \sum_{k_x k_y} \sum_{k'_x k'_y} e^{-i\vec{k}'.\vec{r}_{i_x i_y \alpha}} c^{\dagger}_{i_z \vec{k}' \alpha\sigma} t_{i\alpha,j\beta} e^{i\vec{k}.\vec{r}_{j_x j_y \beta}} c_{j_z \vec{k} \beta\sigma} \tag{2.24}$$

As before, we consider only hopping between the same orbital types and nearest-neighbors. These imply that we can write

$$t_{i\alpha,j\alpha} = t_{i_z\alpha,j_z\alpha}(\vec{r}_{i_x i_y} - \vec{r}_{j_x j_y}) = t_{i_z\alpha,j_z\alpha}(\vec{d}) \tag{2.25}$$

where $\vec{d}$ is a two-dimensional lattice vector connecting nearest neighbor unit cells. Then, it useful to replace the unit cell index i with the triplet (i_x, i_y, i_z), such that

$$\sum_i = \sum_{i_x,i_y,i_z} = \sum_{i_x,i_y} \sum_{i_z}. \tag{2.26}$$

Since

$$\frac{1}{N_{k_x k_y}} \sum_{i_x,i_y} e^{i(\vec{k}-\vec{k}')\cdot\vec{r}_{i_x i_y \alpha}} = \delta_{\vec{k},\vec{k}'}, \tag{2.27}$$

then

$$\hat{H}_0 = \sum_{i_z,j_z} \sum_{d} \sum_{\alpha} \sum_{\sigma} \sum_{k_x k_y} c^{\dagger}_{i_z \vec{k} \alpha\sigma} t_{i_z\alpha,j_z\alpha}(\vec{d}) e^{i\vec{k}.\vec{d}} c_{j_z \vec{k} \beta\sigma}. \tag{2.28}$$

We define

$$\epsilon'_{\alpha}(\vec{k}) = \sum_{i_z,j_z} \sum_{d} t_{i_z\alpha,j_z\alpha}(\vec{d}) e^{-i\vec{k}\cdot\vec{d}}, \tag{2.29}$$

so that the Hamiltonian can be written as

$$\hat{H}_0 = \sum_{\vec{k}} \sum_{\sigma} \Psi^{\dagger}_{\vec{k}\sigma} h_0(\vec{k}) \Psi_{\vec{k}\sigma} \tag{2.30}$$

with $\Psi^{\dagger}_{\vec{k}\sigma} = [c^{\dagger}_{1\vec{k}(xy)\sigma}, c^{\dagger}_{1\vec{k}(xz)\sigma}, c^{\dagger}_{1\vec{k}(yz)\sigma}, c^{\dagger}_{2\vec{k}(xy)\sigma}, \ldots, c^{\dagger}_{M\vec{k}(yz)\sigma}]$, where M is the number of $SrTiO_3$ layers, and

$$h_0(\vec{k}) = \begin{bmatrix} \mathbf{E}(\vec{k}) & \mathbf{T} & \ldots & & \\ \mathbf{T} & \mathbf{E}(\vec{k}) & & & \\ & & \ddots & & \\ & & & \mathbf{E}(\vec{k}) & \mathbf{T} \\ & & & \mathbf{T} & \mathbf{E}(\vec{k}) \end{bmatrix}, \tag{2.31}$$

where

$$\mathbf{E}(\vec{k}) = \begin{bmatrix} \epsilon'_{xy}(\vec{k}) & 0 & 0 \\ 0 & \epsilon'_{xz}(\vec{k}) & 0 \\ 0 & 0 & \epsilon'_{yz}(\vec{k}) \end{bmatrix}, \qquad \mathbf{T} = \begin{bmatrix} t^{\perp}_{xy} & 0 & 0 \\ 0 & t^{\parallel}_{xz} & 0 \\ 0 & 0 & t^{\parallel}_{yz} \end{bmatrix}, \tag{2.32}$$

with

$$\epsilon'_{xy}(\vec{k}) = \epsilon_{t_{2g}} - 2t^{\parallel}_{xy}(\cos k_x a + \cos k_y a), \tag{2.33}$$

$$\epsilon'_{xz}(\vec{k}) = \epsilon_{t_{2g}} - 2t^{\parallel}_{xz}\cos k_x a - 2t^{\perp}_{xz}\cos k_y a, \tag{2.34}$$

$$\epsilon'_{yz}(\vec{k}) = \epsilon_{t_{2g}} - 2t^{\perp}_{yz}\cos k_x a - 2t^{\parallel}_{yz}\cos k_y a. \tag{2.35}$$

To compare with the bulk case, we plot the eigenvalues of the noninteracting Hamiltonian, Eq. (2.31), along the k_x-direction for a two layer $SrTiO_3$ film, at $k_y = 0$,

in Fig. 2.4.(b). At the Γ point, the xz and yz bands are degenerate with each other, and the lowest xy band is split from them. This splitting is due to the interface, which disrupts the hopping along the z-axis. This disruption is more important for the xz and yz bands than the xy band, and pushes the xz and yz bands up relative to the xy band. Therefore, this splitting is a feature of the interface [52], and leads the d_{xy} orbitals to be occupied first.

The External Potential Energy $\hat{V}_{ext}$

As we discussed before, there is a potential divergence inside the $LaAlO_3$ due to its polarity (the polar catastrophe). To overcome this divergence, a half-electron per unit cell (σ_s) is transfered from the surface of the $LaAlO_3$ to the interface. Then, the remaining charges at the $LaAlO_3$ surface create an electrostatic potential inside the $SrTiO_3$ film, which is called in our model the *external potential energy*, Fig. 2.5.

We represent the external potential energy as

$$\hat{V}_{\text{ext}} = \sum_{i_z\alpha\sigma} \varphi^{\text{ext}}_{i_z\alpha} \hat{n}_{i_z\alpha\sigma} \tag{2.36}$$

with the charge density operator

$$\hat{n}_{i_z\alpha\sigma} = c^{\dagger}_{i_z\alpha\sigma} c_{i_z\alpha\sigma}, \tag{2.37}$$

and the potential

$$\varphi^{\text{ext}}_{i_z\alpha} = \frac{-\sigma_s e}{2\epsilon_0\kappa}(z_{i_z\alpha} + \lambda), \tag{2.38}$$

where

- $\sigma_s = \frac{0.5e}{a^2}$ is the surface charge density at the top layer of the $LaAlO_3$.
- ϵ_0 is the permittivity constant.

- λ is the thickness of the $LaAlO_3$ film.
- κ is the $SrTiO_3$ dielectric constant. It is known that the $SrTiO_3$ dielectric constant is a complicated function of electric field and temperature, so it is different from layer to layer inside the $SrTiO_3$ film. For simplification, we have fixed κ to a single value in our model. We choose $\kappa = 15$ based on Ref. [53], which claims that this value reproduces the density functional theory band structure.
- $z_{i_z\alpha}$ is the distance from the interface to the orbital α in unit cell i_z.

Because the thickness of the $LaAlO_3$ film, λ, is constant in our model, it shifts the potential by a constant, which can be absorbed in the chemical potential. Therefore, we take

$$\varphi^{\text{ext}}_{i_z\alpha} = \frac{-\sigma_s e}{2\epsilon_0\kappa} z_{i_z\alpha}. \tag{2.39}$$

The Coulomb Interaction Energy $\hat{V}_C$

The Coulomb interaction inside the $SrTiO_3$ thin film is the summation of the electron-electron interaction energy and the electron-ion interaction energy,

$$\hat{V}_C = \hat{V}_{ee} + \hat{V}_{e-ion}. \tag{2.40}$$

The electron-electron interaction energy is

$$\hat{V}_{ee} = \sum_{i\alpha\sigma, j\beta\sigma'} V_{i\alpha,j\beta} \hat{n}_{i\alpha\sigma} \hat{n}_{j\beta\sigma'} \tag{2.41}$$

where the electron-electron potential is

$$V_{i\alpha,j\beta} = \frac{e^2}{4\pi\epsilon_0\kappa} \frac{1}{|\vec{r}_{i\alpha} - \vec{r}_{j\beta}|}, \tag{2.42}$$

and $\hat{n}_{i\alpha\sigma} = c^{\dagger}_{i\alpha\sigma} c_{i\alpha\sigma}$ is the charge density operator for unit cell index i, orbital type α and electron spin σ. We can write $\hat{n}_{i\alpha\sigma}$ as

$$\hat{n}_{i\alpha\sigma} = \langle \hat{n}_{i\alpha\sigma} \rangle + \delta\hat{n}_{i\alpha\sigma}$$

where $\delta\hat{n}_{i\alpha\sigma}$ is the charge fluctuation about the mean value $\langle \hat{n}_{i\alpha\sigma} \rangle$. Let $n_{i\alpha\sigma} = \langle \hat{n}_{i\alpha\sigma} \rangle$ is the charge density for unit cell i, orbital type α and electron spin σ, then

$$\hat{n}_{i\alpha\sigma}\hat{n}_{j\beta\sigma'} = n_{i\alpha\sigma}n_{j\beta\sigma'} + n_{i\alpha\sigma}\delta\hat{n}_{j\beta\sigma'} + n_{j\beta\sigma'}\delta\hat{n}_{i\alpha\sigma} + \delta\hat{n}_{i\alpha\sigma}\delta\hat{n}_{j\beta\sigma'}.$$

In Hatree approximation, the fluctuation in charge density $\delta\hat{n}_{i\alpha\sigma}\delta\hat{n}_{j\beta\sigma'}$ can be ignored. And since,

$$\delta\hat{n}_{i\alpha\sigma} = \hat{n}_{i\alpha\sigma} - \langle \hat{n}_{i\alpha\sigma} \rangle = \hat{n}_{i\alpha\sigma} - n_{i\alpha\sigma}$$

therefore the electron-electron interaction energy is simplified as

$$\hat{V}_{ee} = \sum_{i\alpha\sigma, j\beta\sigma'} V_{i\alpha,j\beta}\hat{n}_{i\alpha\sigma}n_{j\beta\sigma'} \tag{2.43}$$

The electron-ion interaction energy is

$$\hat{V}_{e-ion} = -\sum_{i\alpha\sigma}\sum_{l} Z_l V_{i\alpha,l}\hat{n}_{i\alpha\sigma} \tag{2.44}$$

where

- l is the index of each ion,
- Z_l is the ionic core charge,
- $V_{i\alpha,l}$ is the potential of electron at unit cell i with orbital type α due to the ionic core at location $\vec{R}_l$, which represents as

$$V_{i\alpha,l} = \frac{e^2}{4\pi\epsilon_0\kappa}\frac{1}{|\vec{r}_{i\alpha} - \vec{R}_l|}. \tag{2.45}$$

We substitute Eq. (2.43) and Eq. (2.44) into Eq. (2.40) to obtain the Coulomb energy,

$$\hat{V}_C = \sum_{i\alpha\sigma,j\beta\sigma} V_{i\alpha,j\beta}\hat{n}_{i\alpha\sigma}n_{j\beta\sigma} - \sum_{i\alpha\sigma}\sum_{l} Z_l V_{i\alpha,l}\hat{n}_{i\alpha\sigma}, \tag{2.46}$$

or

$$\hat{V}_C = \sum_{i\alpha\sigma} \hat{n}_{i\alpha\sigma}\phi^{\mathrm{C,tot}}_{i\alpha}, \tag{2.47}$$

with

$$\phi^{\mathrm{C,tot}}_{i\alpha} = \sum_{j\beta\sigma} V_{i\alpha,j\beta}n_{j\beta\sigma} - \sum_{l} V_{i\alpha,l}Z_l. \tag{2.48}$$

We can represent the Coulomb potential $\phi^{\mathrm{C,tot}}_{i\alpha}$ as

$$\phi^{\mathrm{C}}_{i\alpha} = \phi^{bulk}_{\alpha\sigma} + \phi^{\mathrm{C}}_{i\alpha} \tag{2.49}$$

with

$$\phi^{bulk}_{\alpha} = \sum_{j\beta\sigma} V_{i\alpha,j\beta}n^{bulk}_{\beta\sigma} - \sum_{l} V_{i\alpha,l}Z_l, \qquad \phi^{\mathrm{C}}_{i\alpha} = \sum_{j\beta\sigma} V_{i\alpha,j\beta}\delta n_{j\beta\sigma}. \tag{2.50}$$

Here, ϕ^{bulk}_{α} is the potential at the Ti sites far from the interface, and $\phi^{\mathrm{C}}_{i\alpha}$ is the residual Coulomb potential due to the interface. ϕ^{bulk}_{α} shifts the orbital energy at all sites equally, and thus it can be absorbed into $\epsilon_{t_{2g}}$, which is a parameter in our model. Therefore,

$$\phi^{\mathrm{C,tot}}_{i\alpha} \rightarrow \phi^{\mathrm{C}}_{i\alpha} = \sum_{j\beta\sigma} V_{i\alpha,j\beta}\delta n_{j\beta} \tag{2.51}$$

Here, $\delta n_{j\beta\sigma}$ is defined as the difference between the charge density in orbital type β with electron spin σ at unit cell j and the charge density for an orbital of the same type in the bulk. Since, the bulk $SrTiO_3$ is insulator, the t_{2g} orbitals are empty in the bulk, so we have $\delta n_{j\beta\sigma} = n_{j\beta\sigma} - n^{bulk}_{\beta\sigma} \approx n_{j\beta\sigma}$. Thus, the Coulomb potential is

$$\phi^{\mathrm{C}}_{i\alpha} = \sum_{j\beta\sigma} V_{i\alpha,j\beta}n_{j\beta\sigma}. \tag{2.52}$$

To obtain $\phi^{\mathrm{C}}_{i\alpha}$, we assume that each layer has a homogeneous charge distribution. After some algebraic steps, shown in Appendix A, the total potential is

$$\phi^{\mathrm{C}}_{i_z\alpha} = \frac{-e^2 a}{2\epsilon_0 k} \sum_{j_z} \sum_{\beta\sigma} (|i_z - j_z| - j_z) n_{j_z\beta\sigma}, \tag{2.53}$$

where $\phi_{i_z\alpha}$ here is the potential in layer i_z due to the charge distribution in the $SrTiO_3$ film (see Appendix A for its derivation).

The effective Hamiltonian matrix is then

$$h_{HF}(\vec{k}) = \begin{bmatrix} \mathbf{E}(\vec{k}) + \Phi_1 & \mathbf{T} & \dots & & \\ \mathbf{T} & \mathbf{E}(\vec{k}) + \Phi_2 & & & \\ & & \ddots & & \\ & & & \mathbf{E}(\vec{k}) + \Phi_{M-1} & \mathbf{T} \\ & & & \mathbf{T} & \mathbf{E}(\vec{k}) + \Phi_M \end{bmatrix}, \tag{2.54}$$

with

$$\Phi_{i_z} = \begin{bmatrix} \varphi^{\mathrm{ext}}_{i_z xy} + \phi^{\mathrm{C}}_{i_z xy} & 0 & 0 \\ 0 & \varphi^{\mathrm{ext}}_{i_z xz} + \phi^{\mathrm{C}}_{i_z xz} & 0 \\ 0 & 0 & \varphi^{\mathrm{ext}}_{i_z yz} + \phi^{\mathrm{C}}_{i_z yz} \end{bmatrix}, \tag{2.55}$$

where i_z takes values from 1 to M, the number of $SrTiO_3$ layers. This means that when $i_z = 1$, we obtain the matrix Φ_1 and so on. Then the effective Hamiltonian can be diagonalized numerically to obtain eigenvalues, $\varepsilon_{n\vec{k}}$, and eigenvectors, $\psi_{i_z\alpha n}(\vec{k})$. From this, the charge density, whose derivation is shown in Appendix B, may be calculated as

$$n_{j_z\beta\sigma} = \frac{1}{N} \sum_{\vec{k}} \sum_{n} |\psi_{j_z\beta\sigma,n}(\vec{k})|^2 f(\varepsilon_{n\vec{k}}) \tag{2.56}$$

where

- n is the band index.
- $\psi_{j_z\beta\sigma n}(\vec{k})$ is the nth eigenvector of the $SrTiO_3$ Hamiltonian.
- $f(\varepsilon_{nk})$ is the Fermi-Dirac distribution function, which is

$$f(\varepsilon_{n\vec{k}}) = \frac{1}{2}[1 - \tanh(\frac{1}{2k_BT}(\varepsilon_{n\vec{k}} - \mu))], \tag{2.57}$$

  where k_B is the Boltzmann constant and T is the temperature of the $SrTiO_3$ film system in Kelvin.

Finally, the Coulomb energy is

$$\hat{V}_C = \frac{-e^2a}{2\epsilon_0 k}\sum_{i_z\alpha\sigma}\sum_{j_z}\sum_{\beta}(|i_z - j_z| - j_z)n_{j_z\beta\sigma}\hat{n}_{i_z\alpha\sigma} \tag{2.58}$$

As we see from Eq. (2.58), to calculate the total interaction energy of the electrons, we need to know the charge density $n_{j_z\beta\sigma}$. To get that, we perform the self-consistency calculations according to flowchart shown in Fig. 2.6. These calculations yield the self-consistent potential which is used to calculate the $SrTiO_3$ Hamiltonian. The self-consistent results will discussed in details in the next chapter.

2.2.3 Impurities at the $LaAlO_3/SrTiO_3$ Interface

The goal of this section is to calculate the interface conductivity. As is well-known, the conductivity is related to the scattering rate due to impurities. Thus, we include impurities in our model and calculate the resultant scattering rate. To understand the many-impurity problem, we start by including a single impurity. In this case the tight-binding Hamiltonian is

$$\hat{H}_{tot} = \hat{H} + \hat{H}_{imp} \tag{2.59}$$

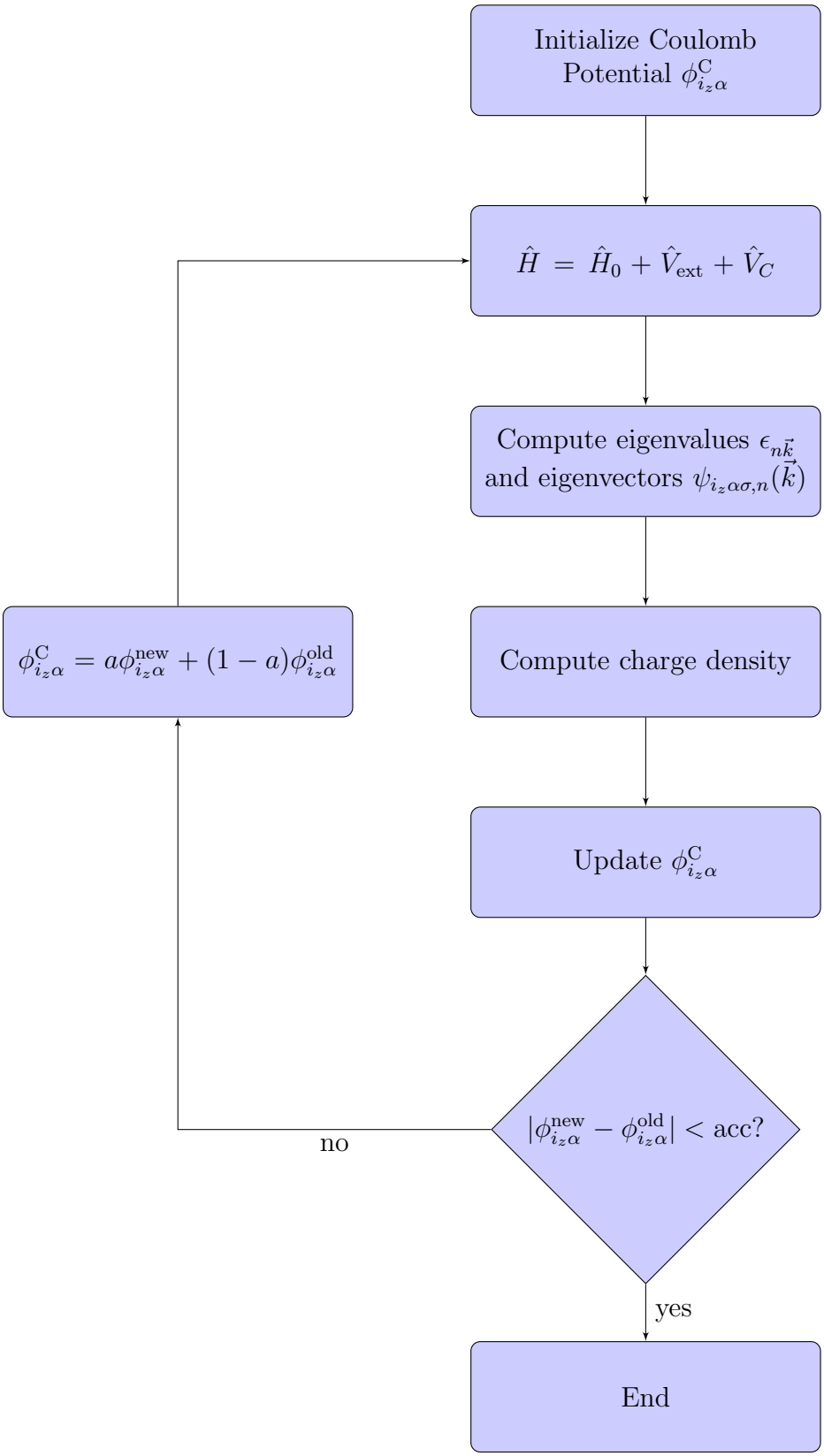

Figure 2.6: Flowchart of the self-consistent calculations.

where $\hat{H}$ is the $SrTiO_3$ thin film Hamiltonian shown in Eq. (2.18), and $\hat{H}_{imp}$ is the perturbation due to an impurity at site i [54],

$$\hat{H}_{imp} = \sum_{\alpha\sigma} \tilde{V}_{\text{imp}} c^{\dagger}_{i\alpha\sigma} c_{i\alpha\sigma}, \tag{2.60}$$

where $i = (i_x, i_y, i_z)$ is the impurity site. We have two-dimensional translational invariance in the model, thus we get the same answer for any (i_x, i_y). Economou [54] solves the total Hamiltonian by finding the corresponding Green function G, which in the case of one impurity is

$$G_{u\alpha,v\beta}(\omega) = G^0_{u\alpha,v\beta}(\omega) + G^0_{u\alpha,i\alpha}(\omega) T_{i\alpha,i\alpha}(\omega) G^0_{i\alpha,v\beta}(\omega), \tag{2.61}$$

where $u\alpha$ and $v\beta$ are site/orbital indices. G^0 is the Green function corresponding to $\hat{H}$, and the t-matrix $T_{i\alpha,i\alpha}(\omega)$ gives the exact correction to the Green function due to the impurity of site i. If an impurity is in layer i_z with potential $\tilde{V}_{\text{imp}}$, then the t-matrix as a function of energy ω [54] is

$$T_{i_z\alpha,i_z\alpha}(\omega) = \frac{\tilde{V}_{\text{imp}}}{1 - \tilde{V}_{\text{imp}} g^0_{i_z\alpha,i_z\alpha}(\omega)}, \tag{2.62}$$

with

$$g^0_{i_z\alpha,i_z\alpha}(\omega) = \frac{1}{N_k} \sum_k G^0_{i_z\alpha,i_z\alpha}(\omega, \vec{k}), \tag{2.63}$$

is the local Green function, and

$$G^0_{i_z\alpha,i_z\alpha}(\omega, \vec{k}) = \sum_n |\psi_{i_z\alpha,n}(\vec{k})|^2 \frac{1}{\omega + i\eta - \varepsilon_n(\vec{k})}, \tag{2.64}$$

where η is a positive infinitessimal number.

In the case of a non-zero density of impurities, we use the average t-matrix approximation, which is discussed by Economou [55]. This approximation neglects interference which is caused by multiple scattering from impurities. Thus the Green

function in matrix representation is

$$\mathbf{G}(\omega,\vec{k}) = \mathbf{G}^0(\omega,\vec{k}) + \mathbf{G}^0(\omega,\vec{k})\mathbf{\Sigma}(\omega)\mathbf{G}(\omega,\vec{k}), \tag{2.65}$$

where boldface symbols indicate matrices with rows $i_z\alpha$, and columns $j_z\beta$. $\mathbf{\Sigma}$ is the self-energy, and in the case of low impurity density c (the dilute limit),

$$\Sigma_{i_z\alpha,j_z\beta}(\omega) = cT_{i_z\alpha,i_z\alpha}(\omega)\delta_{i_z\alpha,j_z\beta}. \tag{2.66}$$

For convenience, we transform the self-energy to the band basis, and neglect inter-band scattering by impurities. Thus

$$\Sigma_n(\omega,\vec{k}) = c\sum_{i_z\alpha} |\psi_{i_z\alpha n}(\vec{k})|^2 T_{i_z\alpha,i_z\alpha}(\omega). \tag{2.67}$$

Since $\psi_{i_z\alpha n}$ doesn't depend on $\vec{k}$ in our model, the self-energy at $\vec{k}$ is the same as at the Γ point,

$$\Sigma_n(\omega) = c\sum_{i_z\alpha} |\psi_{i_z\alpha n}(\Gamma)|^2 T_{i_z\alpha,i_z\alpha}(\omega). \tag{2.68}$$

The scattering rate for electrons in band n is given in terms of the self-energy [56] as

$$\gamma^n(\omega) = -Im\Sigma_n(\omega). \tag{2.69}$$

Thus, in terms of the t-matrix, the scattering rate is

$$\gamma^n(\omega) = -cIm\sum_{i_z\alpha} |\psi_{i_z\alpha n}(\Gamma)|^2 T_{i_z\alpha,i_z\alpha}(\omega). \tag{2.70}$$

From Eq. (2.70), we can obtain the conductivity under the assumption that there is a low density of point-like impurities at the $LaAlO_3/SrTiO_3$ interface. This means

$T_{i_z\alpha,i_z\alpha}(\omega) = 0$ unless $i_z = 1$, and thus the scattering is

$$\gamma^n(\omega) = -cIm \sum_{\alpha} |\psi_{1\alpha n}(\Gamma)|^2 T_{1\alpha,1\alpha}(\omega). \tag{2.71}$$

Derivation of The Interface Conductivity

We begin our derivation by using Ashcroft and Mermin's Eq. (13.24) and Eq. (13.25) for the semi-classical DC conductivity tensor σ [57]. They derived σ under some assumptions: they neglect inter-band transitions, assume the system temperature is uniform, and that the electric field and temperature don't change with time. Thus the three-dimensional conductivity is

$$\sigma_{3D} = \sum_{n} \sigma_{3D}^{(n)}, \tag{2.72}$$

where $\sigma_{3D}^{(n)}$ is the contribution of band n to the three-dimensional conductivity,

$$\sigma_{3D}^{(n)} = e^2 \int \frac{d\mathbf{k}}{4\pi^3} \tau_n(\varepsilon_n(\mathbf{k})) \mathbf{v}_n(\mathbf{k}) \mathbf{v}_n(\mathbf{k}) (-\frac{\partial f}{\partial \varepsilon})_{\varepsilon=\varepsilon_n(\mathbf{k})}, \tag{2.73}$$

where

- $\tau_n(\varepsilon_n(\mathbf{k}))$ is the collision time, which is independent of k in our model and equals $\hbar/\gamma^{(n)}(\varepsilon_f)$, and ε_f is the Fermi energy.
- $\mathbf{v}_n(\mathbf{k})$ is the velocity of electrons and equals $\frac{1}{\hbar}\frac{\partial \varepsilon_n(\mathbf{k})}{\partial \mathbf{k}}$.

The two-dimensional conductivity, $\sigma_{2D}^{(n)}$ is obatained by a simple modification of Eq. (2.73),

$$\sigma_{2D}^{(n)} = e^2 \tau_n \int \frac{d^2k}{2\pi^2} \mathbf{v}_n(\vec{k}) \mathbf{v}_n(\vec{k}) (-\frac{\partial f}{\partial \varepsilon})_{\varepsilon=\varepsilon_n(\vec{k})}. \tag{2.74}$$

Figure 2.7 shows the Fermi function at $T = 0$ and it's derivative $\frac{-\partial f}{\partial \varepsilon}$. As shown, $\frac{-\partial f}{\partial \varepsilon}$ is a $\delta-$function peaked at ε_f. Therefore,

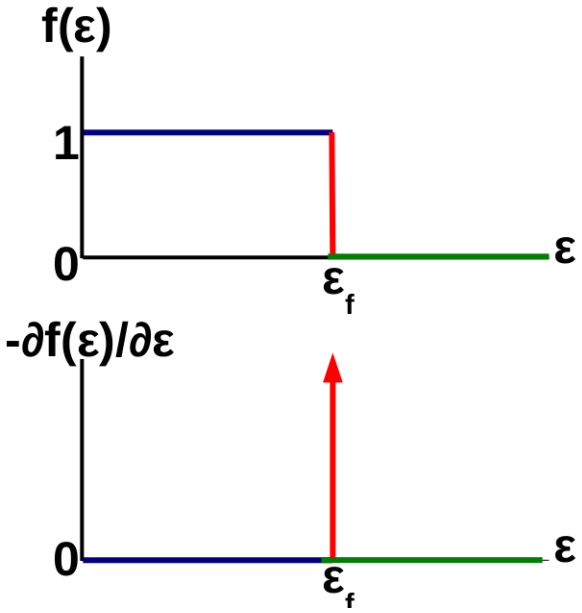

Figure 2.7: Fermi function at $T = 0$ and its derivative.

$$\sigma_{2D}^{(n)} = \frac{e^2\tau_n}{2\pi^2}\int d^2k \mathbf{v}_n(\vec{k})\mathbf{v}_n(\vec{k})\delta(\varepsilon_n - \varepsilon_f). \tag{2.75}$$

Here, we focus on the conductivity σ_{xx}, so we need the v_x-compound for band n,

$$v_{nx}(\vec{k}) = \frac{1}{\hbar}\frac{\partial\epsilon_n(\vec{k})}{\partial k_x}. \tag{2.76}$$

To obtain a simple expression for the conductivity, we approximate the dispersions near the Γ point by their quadratic forms

$$\epsilon_n(\vec{k}) = \frac{\hbar^2}{2}(\frac{k_x^2}{m_x^n} + \frac{k_y^2}{m_y^n}) + \varepsilon_{n0}, \tag{2.77}$$

where ε_{n0} is the band bottom energy, which comes from the self-consistent bands at the Γ point, and m_x^n and m_y^n are the effective masses in the x- and y-direction, respectively. The effective mass m^* is

$$\frac{1}{m_{x,y}^*} = \frac{1}{\hbar^2}\frac{d^2\epsilon_n(\vec{k})}{d^2k_{x,y}}|_{\vec{k}=0}, \tag{2.78}$$

so by using Eqs. (2.33), (2.34) and (2.35), the approximate effective masses in the x and y directions for the xy bands are

$$m_x^{xy} = m_y^{xy} = \frac{\hbar^2}{2at^{\parallel}}, \tag{2.79}$$

for the xz bands are

$$m_x^{xz} = \frac{\hbar^2}{2at^{\parallel}}, \qquad m_y^{xz} = \frac{\hbar^2}{2at^{\perp}}, \tag{2.80}$$

and for the yz band are

$$m_x^{yz} = \frac{\hbar^2}{2at^{\perp}}, \qquad m_y^{yz} = \frac{\hbar^2}{2at^{\parallel}}. \tag{2.81}$$

To calculate the integral over $\vec{k}$, we let

$$\xi_x = \frac{\hbar k_x}{\sqrt{m_x}}, \qquad \xi_y = \frac{\hbar k_y}{\sqrt{m_y}}. \tag{2.82}$$

This gives

$$\int d^2k \to \frac{\sqrt{m_x m_y}}{\hbar^2} \int d\xi_x \xi_y \to \frac{\sqrt{m_x m_y}}{\hbar^2} \int_0^{2\pi} d\theta \int_0^{\infty} \xi d\xi. \tag{2.83}$$

Then

$$v_{nx} = \frac{1}{\sqrt{m_x}} \xi_x = \frac{1}{m_x} \xi^2 \cos^2\theta. \tag{2.84}$$

The two dimensional band conductivity in the $x-$direction is

$$\sigma_{xx}^{(n)} = \frac{e^2 \tau_n}{2\pi^2} \frac{\sqrt{m_x^n m_y^n}}{\hbar^2} \int_0^{2\pi} d\theta \int_0^{\infty} \xi d\xi \frac{1}{m_x^n} \xi^2 \cos^2\theta \delta(\varepsilon_n - \varepsilon_f), \tag{2.85}$$

or

$$\sigma_{xx}^{(n)} = \frac{e^2 \tau_n}{4\pi^2 \hbar^2} \sqrt{\frac{m_y^n}{m_x^n}} \int \xi d\xi \xi^2 \delta(\varepsilon_n - \varepsilon_f). \tag{2.86}$$

Since,

$$\varepsilon_n - \varepsilon_{n0} = \frac{\xi^2}{2}, \tag{2.87}$$

and

$$d\varepsilon_n = \xi d\xi. \tag{2.88}$$

Therefore,

$$\sigma_{xx}^{(n)} = \frac{e^2\tau_n}{4\pi^2\hbar^2}\sqrt{\frac{m_y^n}{m_x^n}}\int_{\varepsilon_{n0}}^{\infty} d\varepsilon_n(\varepsilon_n - \varepsilon_{n0})\delta(\varepsilon_n - \varepsilon_f). \tag{2.89}$$

Finally,

$$\sigma_{xx}^{(n)} = \frac{e^2\tau_n}{4\pi^2\hbar^2}\sqrt{\frac{m_y^n}{m_x^n}}(\varepsilon_f - \varepsilon_{n0}), \tag{2.90}$$

or

$$\sigma_{xx}^{(n)} = \begin{cases} \frac{e^2}{4\pi^2\hbar^2}\sqrt{\frac{m_y^n}{m_x^n}}\frac{\epsilon_f^n}{\gamma^n} & \text{when } \epsilon_f^n > 0, \\ 0 & \text{when } \epsilon_f^n < 0, \end{cases} \tag{2.91}$$

with $\varepsilon_f^n = (\varepsilon_f - \varepsilon_{n0})$.

Summing over occupied bands gives

$$\sigma_{xx} = \frac{e^2}{4\pi^2\hbar^2}\sum_n{}' \sqrt{\frac{m_y^n}{m_x^n}}\frac{\epsilon_f^n}{\gamma^n}, \tag{2.92}$$

where $\sum'$ is only over occupied bands.

As we see from Eq. (2.91), the band conductivity depends on the impurity potential $\tilde{V}_{\text{imp}}$ and impurity density c. For the dilute limit assumption, the scattering rate is linearly proportional to c. Thus, to remove the dependence on c, we calculate the fractional conductivity

$$\frac{\sigma_{xx}^{(n)}(\tilde{V}_{\text{imp}})}{\sigma_{xx}(\tilde{V}_{\text{imp}})} = \frac{\sqrt{\frac{m_y^n}{m_x^n}}\frac{\epsilon_f^n}{\gamma^n}}{\sum_n{}' \sqrt{\frac{m_y^n}{m_x^n}}\frac{\epsilon_f^n}{\gamma^n}}. \tag{2.93}$$

Equation (2.93) gives the relative contribution of each occupied band to the two-dimensional conductivity as a function in $\tilde{V}_{\text{imp}}$. As shown, there are three parameters that control the fractional conductivity: the impurity potential, the effective mass ratios, and the filling. In the next chapter, we will discuss how these parameters

affect the interface conductivity in detail.

Chapter 3

Results and Discussion

3.1 Introduction

In this chapter, we will discuss the results of calculations based on the $LaAlO_3/SrTiO_3$ interface model. We model the $SrTiO_3$ as a thin film. To choose the proper $SrTiO_3$ film thickness, we calculated the self-consistent charge density for different $SrTiO_3$ thicknesses.

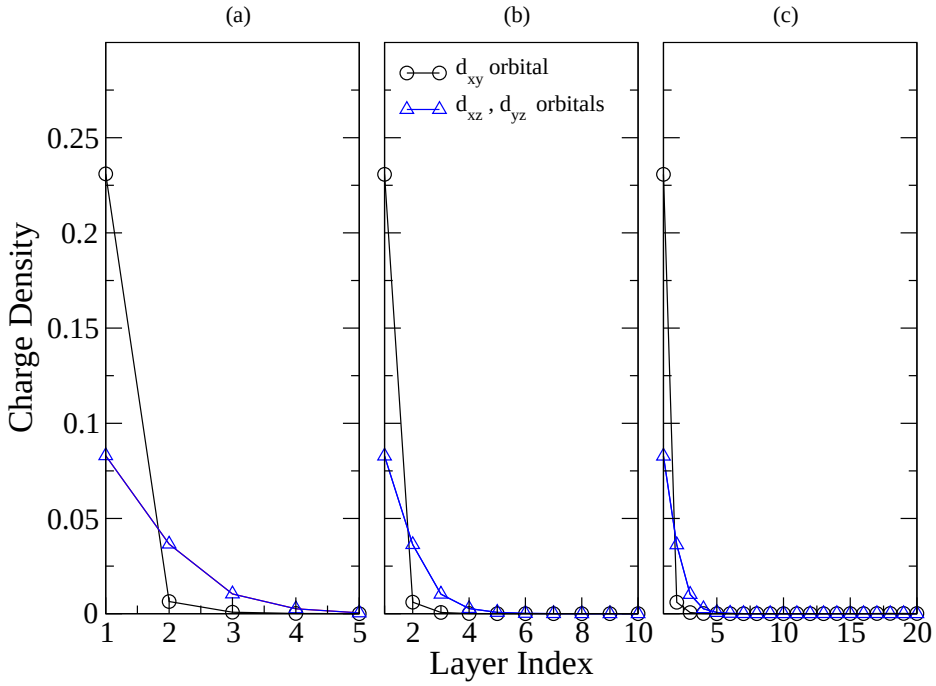

Figure 3.1: The calculated self-consistent charge density for different $SrTiO_3$ thicknesses: (a) 5 layers, (b) 10 layers and (c) 20 layers.

As shown in Fig. 3.1, the charge density is vanishingly small after the fifth or sixth layer in the $SrTiO_3$ film. Hence, we decided to make all our model calculations using a 10 layer film. Table 3.1 shows the model parameters used in our calculations.

We will discuss the self-consistent calculations and compare them with previously published calculations. Then, we will discuss the results for the interface conductivity.

Parameter	**Value**
$SrTiO_3$ lattice constant a	3.904 $\mathring{A}$
$SrTiO_3$ dielectric constant κ	15 [53]
System temperature T	90 K [49]
Parallel hopping terms $t^{\parallel}$	236 meV [49]
Perpendicular hopping terms $t^{\perp}$	35 meV [49]
On-site t_{2g} orbital energy $\epsilon_{t_{2g}}$	0.0 eV

Table 3.1: Model parameters used in the calculations.

3.2 Self-consistent Calculations

Our model assumes that the electronic reconstruction is the only mechanism for the 2DEG formation at the interface. Thus, as we discussed before, a half-electron per unit cell is transfered from the top layer of $LaAlO_3$ to the $SrTiO_3$ film. This is the starting point in the self-consistent calculations; we run the self-consistency code for different chemical potential values μ until the total charge density inside the $SrTiO_3$ is a half-electron per 2D unit cell.

Figure 3.2 shows the self-consistent potential and charge density in the $SrTiO_3$ thin film, and the resultant band structure is shown in Fig. 3.3. After the fourth layer, as shown in Fig. 3.2(a), when the charge density inside the $SrTiO_3$ thin film equals a half-electron per 2D unit cell, the electric field due to the $SrTiO_3$ cancels the electric field due to the surface charge density at the $LaAlO_3$ top layer. Thus the total potential inside the $SrTiO_3$ thin film is nearly constant after the fourth layer. The potential forms a quantum well in the first four layers, with approximately 0.4eV depth, which confines the electrons to the interface; consequently, most of the charge ($\approx 78\%$) is concentrated in the first $SrTiO_3$ layer, as shown in Fig. 3.2(b).

Figure 3.2(b) shows the charge density in each orbital type (d_{xy}, d_{xz} and d_{yz}) as a function of layer index. The d_{xy} orbital in the first layer has most of the total charge density ($\approx 46\%$), while the d_{xy} orbital in the second layer is only slightly

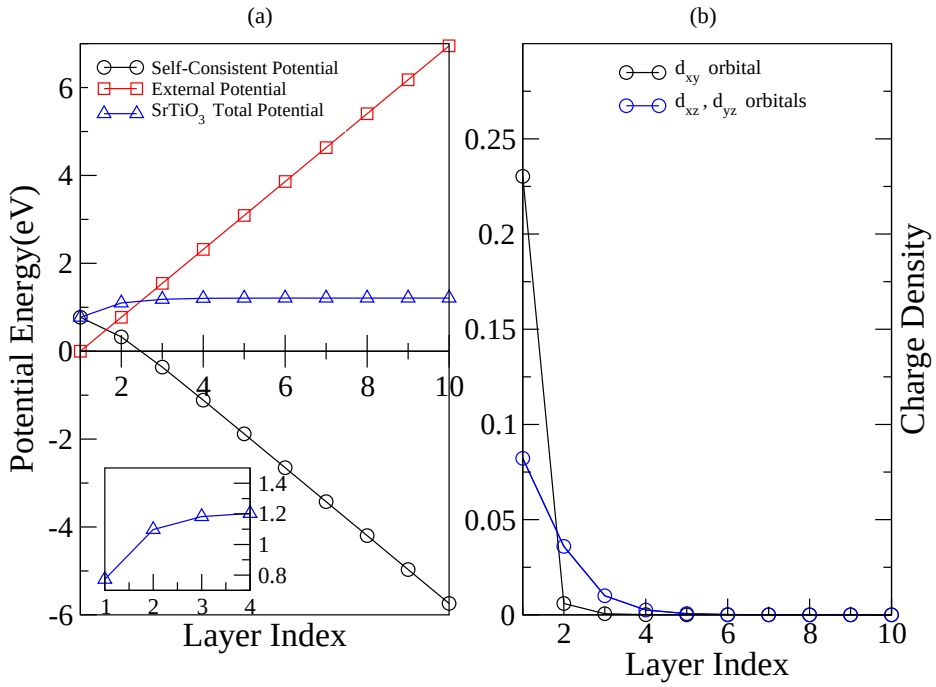

Figure 3.2: The self-consistent solutions for (a) the total potential energy and (b) the charge density inside the $SrTiO_3$ thin film. The total charge density is 0.50 electrons per 2D unit cell. The chemical potential is $\mu = 0.15$eV. Inset shows the total potential in the first four layers.

occupied, and the remaining d_{xy} orbitals are nearly empty. The d_{xz} and d_{yz} orbitals have identical charge density distributions, contributing together about 32% of the total charge density in the first layer. The charge density extends smoothly until the fifth layer and is negligible after that.

Figure 3.3 shows the self-consistent band structure for the 10 layer $SrTiO_3$ film. The band structure is plotted along Γ-X and Γ-M in the Brillouin zone (shown in the inset Fig. 3.3). Along X-Γ, there are four bands below the Fermi level: the $1xy$ band has the lowest energy, which is a signature of the interface; the $1xz$ and $1yz$ bands, which are degenerate at the Γ point, disperse differently away from it, with more dispersion for the $1xz$ band; the $2xy$ band is a little below the Fermi level at the Γ point. The features are similar to what was found in Fig. 2.4(b) for the non

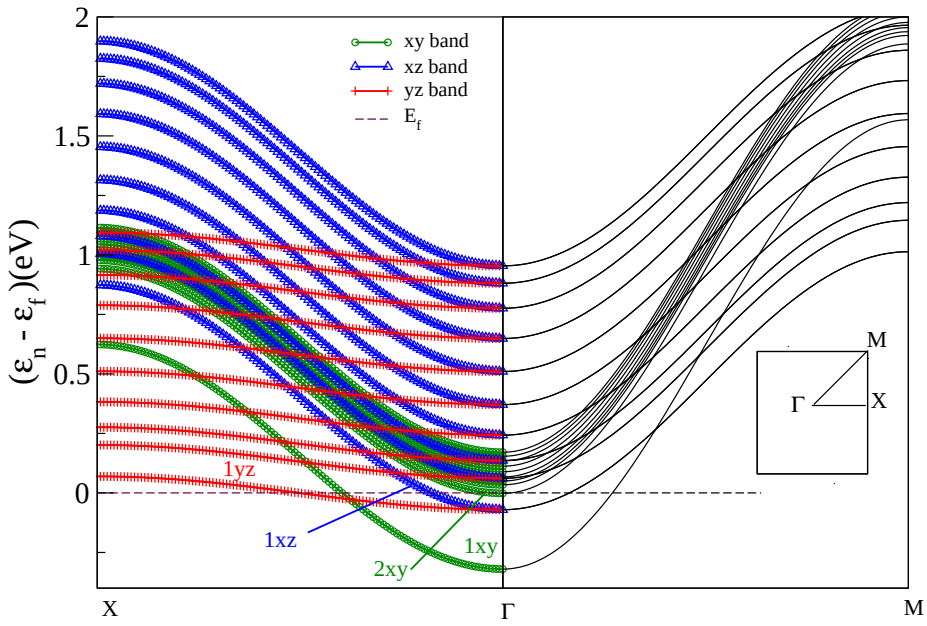

Figure 3.3: The self-consistent band structure for a 10 layer $SrTiO_3$ thin film along $\Gamma - X$ and $\Gamma - M$ directions. The total charge density is 0.50 electrons per 2D unit cell. The chemical potential is $\mu = 0.15$eV. Inset shows the Brillouin zone with Γ, X, and M points indicated.

interacting model, except that here, the splitting between the $1xy$ and $2xy$ bands is much bigger than in Fig. 2.4(b) due to the quantum well at the interface. Along Γ-M, the same four bands cross the Fermi level, but the $1xz$ and $1yz$ bands are completely degenerate.

Figure 3.4 plots the Fermi surfaces at the Fermi energy ($E_f = 0.15$eV) in the k_x-k_y plane. As shown, there are two circles corresponding to the $1xy$ and $2xy$ bands, and two ellipses for the $1xz$ and $1yz$ bands. Also, we note that the area of the $2xy$ Fermi surface, which gives the band occupation, is very small because the bottom of $2xy$ band lies just 0.001eV below the Fermi energy.

We have calculated the projected band weights (PBW) $\psi^2_{i_z\alpha,n}(\Gamma)$ of the four occupied bands at the Γ point, where $\psi_{i_z\alpha,n}$ is the eigenvector of the $SrTiO_3$ thin film Hamiltonian. In general, the PBW depends on $\vec{k}$, however, in our model it does not.

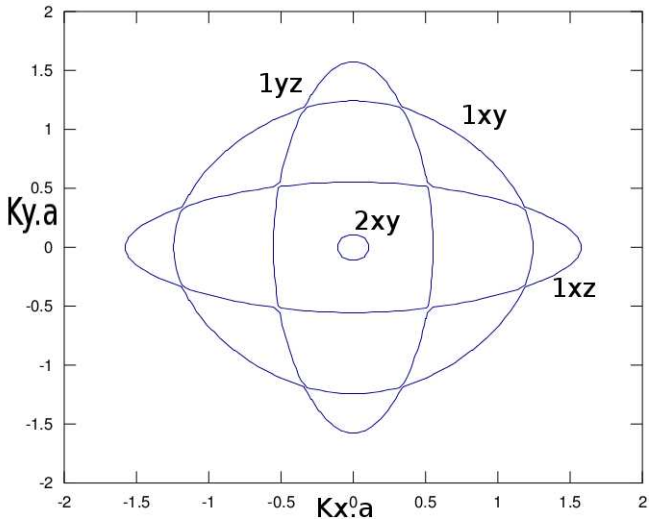

Figure 3.4: Fermi surfaces for a Fermi energy $E_f = 0.15$eV.

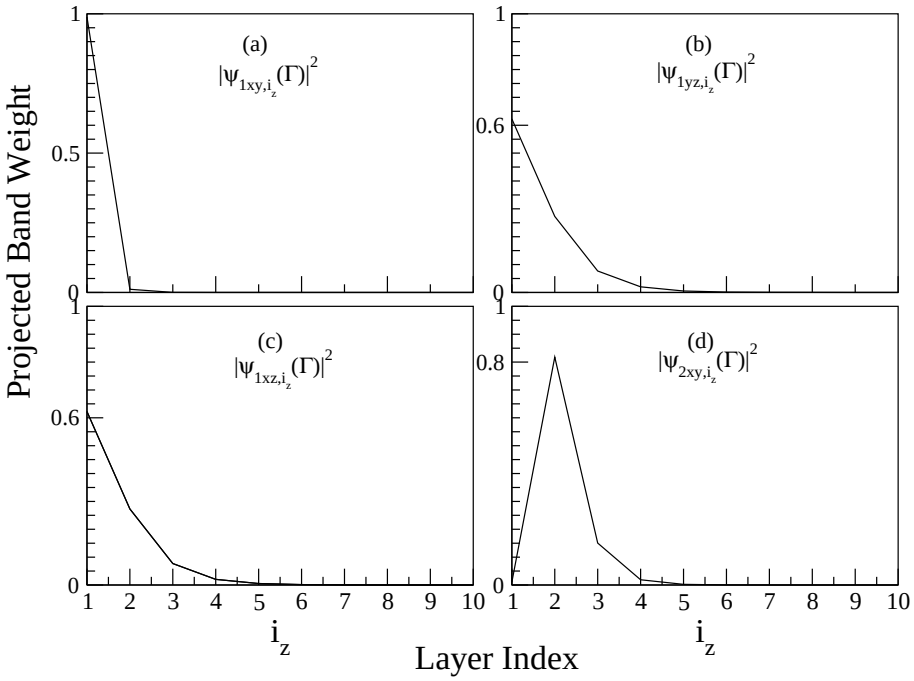

Figure 3.5: The projected weight of the first four bands in Fig. 3.3. (a) the band weight for $1xy$ band, (b) the band weight for $1yz$ band, (c) the band weight for $1xz$ band, and (d) the band weight for $2xy$ band.

The PBW is shown in Fig. 3.5. In Fig. 3.5(a), the lowest band has d_{xy} character, and its projected weight comes almost entirely from the first layer and drops quickly

along z-axis. This explains the distribution of the d_{xy} charge density shown in Fig. 3.2(b) because most of the charge density resides in the $1xy$ band. This behaviour implies that the $1xy$ band forms a strongly two-dimensional electron gas (2DEG) at the interface.

The second and third bands have d_{yz} and d_{xz} orbital character, respectively. In Figs. 3.5(b) and (c), they have about 60% of their weight in the first layer, and spread along the z-axis out to the sixth layer. This behaviour is the same as the distribution of the charge density in the d_{yz} and d_{xz} orbitals in Fig. 3.2(b). This shows that the charge density is less confined than in the $1xy$ band. This leads the $1xz$ and $1yz$ bands to be less affected by impurities at the interface than the $1xy$ band.

By referring to Eq. (2.54), the difference between the $1xy$, $1xz$ and $1yz$ bands can be explained. The hopping along the z-direction for the d_{xz} and d_{yz} orbitals is proportional to the parallel hopping term $t^{\|}$, while the hopping between the d_{xy} orbitals is proportional to the perpendicular hopping term $t^{\perp}$. Since $t^{\|} \gg t^{\perp}$, the $1xz$ and $1yz$ bands are much lighter than the $1xy$ band along the z-direction, and the $1xz$ and $1yz$ bands are less confined by the quantum well than the $1xy$ band.

Figure 3.5(d) shows the weight of the $2xy$ band. Its projected weight comes mostly from the second layer (80%) and spreads for a few layers along the z-axis. Here, we note that the $2xy$ band spreads along the z-axis more than the $1xy$ band because it is higher energy and consequently it is less confined by the quantum well than the $1xy$ band.

The self-consistent band structures in Fig. 3.3 are compatible with published band structure calculations [58]: the lowest band has xy character, the yz bands have small dispersion along X-Γ direction, the splitting between $1xy$, and $1yz$ bands is nearly 0.25eV, and the energy difference between the lowest two xy bands is about 0.3eV. However, there is a difference between the band structure in Fig. 3.3 and that in Ref.

[58]: the energy difference between the bottom of lowest band, the $1xy$ band, and the Fermi level is slightly bigger in [58] than that in Fig. 3.3. This leads Ref. [58] to have more xy Fermi surfaces than in Fig. 3.4. We note that the Fermi surface structure is highly sensitive to details and has not been fully resolved.

The band structure in Fig. 3.3 is consistent with experimental study [59]. Ref. [59] used x-ray absorption spectroscopy to investigate the $LaAlO_3/SrTiO_3$ electronic properties, and found that the lowest band has xy character, and that there is no degeneracy around the Γ point between the xy, and yz or xz bands, as in Fig. 3.3.

We find also that self-consistent charge density calculations agree with previous calculations [60]. Ref. [60] used the first-principles density functional method to calculate the charge density for a 7.5 and 8.5 layer $SrTiO_3$ film. They found that the d_{xy} electrons make the major contribution to the charge density profile and extend only 2 or 3 layers into the $SrTiO_3$ film, as in Fig. 3.2. Also, they showed that the d_{xz} and d_{yz} charge density spread through the $SrTiO_3$ film and have the same density profile, as in Fig. 3.2. The agreements between our model and published work shows that, while simple, our model captures the essential features of the $LaAlO_3/SrTiO_3$ interface.

3.3 Impurities at the $LaAlO_3/SrTiO_3$ Interface

We now discuss what happens when we include impurities at the $LaAlO_3/SrTiO_3$ interface. In chapter 2, we obtained an equation for the two dimensional band conductivity, (2.91). As we mentioned before, this equation is a function of two variables: the impurity density c and the impurity potential $\tilde{V}_{\rm imp}$. For dilute impurities, the conductivity is a function of $1/c$. To remove the dependence on c, we calculate the

Band	$\sqrt{\frac{m_y}{m_x}}$	ϵ_f^n (eV)
$1xy$	1	0.319
$1yz$	0.385	0.069
$1xz$	2.597	0.069
$2xy$	1	0.001

Table 3.2: The ratio of effective masses in the x- and y-directions, $\sqrt{\frac{m_y}{m_x}}$, for the four occupied bands, and their band filling, ϵ_f^n. Data are for the case where the $SrTiO_3$ film is 10 layers thick.

fractional conductivity (2.93),

$$\frac{\sigma_{xx}^{(n)}(\tilde{V}_{\rm imp})}{\sigma_{xx}(\tilde{V}_{\rm imp})} = \frac{\sqrt{\frac{m_y^n}{m_x^n}}\frac{\epsilon_f^n}{\gamma^n}}{\sum_n' \sqrt{\frac{m_y^n}{m_x^n}}\frac{\epsilon_f^n}{\gamma^n}}. \tag{3.1}$$

which gives the contribution of each occupied band to the total two dimensional conductivity as a function of $\tilde{V}_{\rm imp}$. From Figs. 3.3 and 3.4, there are four occupied bands, two with d_{xy} orbital character, and one each with d_{xz} and d_{yz} orbital character.

There are three parameters in Eq. (3.1) which control the contribution of each band to the total two dimensional conductivity. These parameters are the ratio of effective masses in the x- and y-directions for each band (Table 3.2), the difference ϵ_f^n between the Fermi energy and band bottom, and the scattering rate γ^n for each band (plotted in Fig. 3.6). We will discuss in detail the role of these parameters in the fractional conductivity. First, we will study how the scattering rate for occupied bands behaves as a function of impurity potential $\tilde{V}_{\rm imp}$. This will require a discussion of the t-matrix and how it relates to the local Green function. Then, we will study how the scattering rate, along with the other parameters, affects the fractional conductivity.

The first step to understand the fractional conductivity is to look at the scattering rate. Figure 3.6 gives the scattering rates for the four occupied bands as a function of $\tilde{V}_{\rm imp}$ for a 10 layer $SrTiO_3$ film. As shown, the $1xy$ band has the biggest scattering

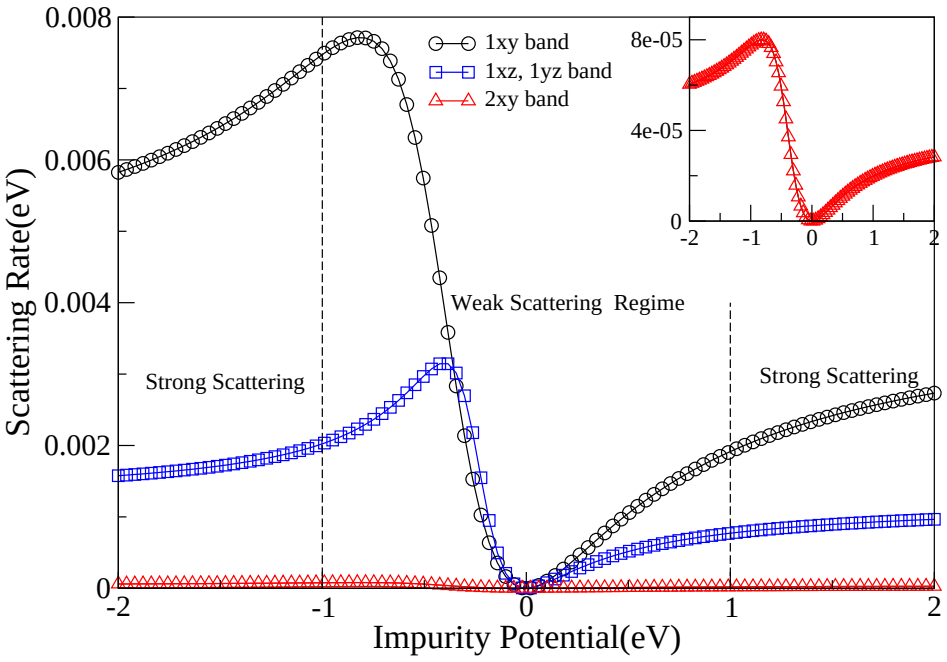

Figure 3.6: The scattering rates as a function of $\tilde{V}_{\rm imp}$ for occupied bands: the $1xy$ band, the $1xz$ band, the $1yz$ band, and the $2xy$. The $SrTiO_3$ film thickness is 10 layers.

rate, while the $2xy$ has the lowest one. The $1xz$ and $1yz$ have identical scattering rates. We note also that all the bands have similar dependences on the impurity potential $\tilde{V}_{\rm imp}$, and we can divide this dependence into two regimes: a weak scattering regime, $-1\text{eV} \lesssim \tilde{V}_{\rm imp} \lesssim 1\text{eV}$, and strong scattering regime, $\tilde{V}_{\rm imp} \gtrsim 1\text{eV}$ or $\tilde{V}_{\rm imp} \lesssim -1\text{eV}$.

To analyze Fig. 3.6, we refer to Eq. (2.70),

$$\gamma^n(\omega) = -c \sum_\alpha |\psi_{1\alpha n}(\Gamma)|^2 \text{Im } T_{1\alpha,1\alpha}(\omega). \tag{3.2}$$

Equation (3.2) then shows that γ^n is proportional to the projected weight $|\psi_{1\alpha n}(\Gamma)|^2$. As shown in Fig 3.5, the projected band weight for the four occupied bands is different at the first layer. This explains in part why the $1xy$, $2xy$, and $1xz$ bands have different scattering rates, while the scattering rate of the $1xz$ and $1yz$ bands are identical.

To understand the dependence of scattering rate on $\tilde{V}_{\rm imp}$, we have to look at the

detailed structure of t-matrix. Since the t-matrix, Eq. (2.62), is

$$T_{i_z\alpha,i_z\alpha}(\omega) = \frac{\tilde{V}_{\rm imp}}{1 - \tilde{V}_{\rm imp} g^0_{i_z\alpha,i_z\alpha}(\omega)}, \tag{3.3}$$

then the imaginary part of the t-matrix is

$$T''_{i_z\alpha,i_z\alpha}(\omega) = \frac{g^{0\prime\prime}_{i_z\alpha,i_z\alpha}(\omega)}{(V^{-1}_{\rm imp} - g^{0\prime}_{i_z\alpha,i_z\alpha}(\omega))^2 + (g^{0\prime\prime}_{i_z\alpha,i_z\alpha}(\omega))^2}, \tag{3.4}$$

where, $g^{0\prime\prime}_{i_z\alpha,i_z\alpha}$ and $g^{0\prime}_{i_z\alpha,i_z\alpha}$ are the imaginary and real parts of $g^0_{i_z\alpha,i_z\alpha}(\omega)$, respectively. Equation (3.4) is plotted in Figs. 3.7 and 3.8 at two specific $\tilde{V}_{\rm imp}$ values, $\tilde{V}_{\rm imp} = -0.2$eV and $\tilde{V}_{\rm imp} = -1.5$eV. These correspond to the weak scattering and strong scattering cases mentioned previously.

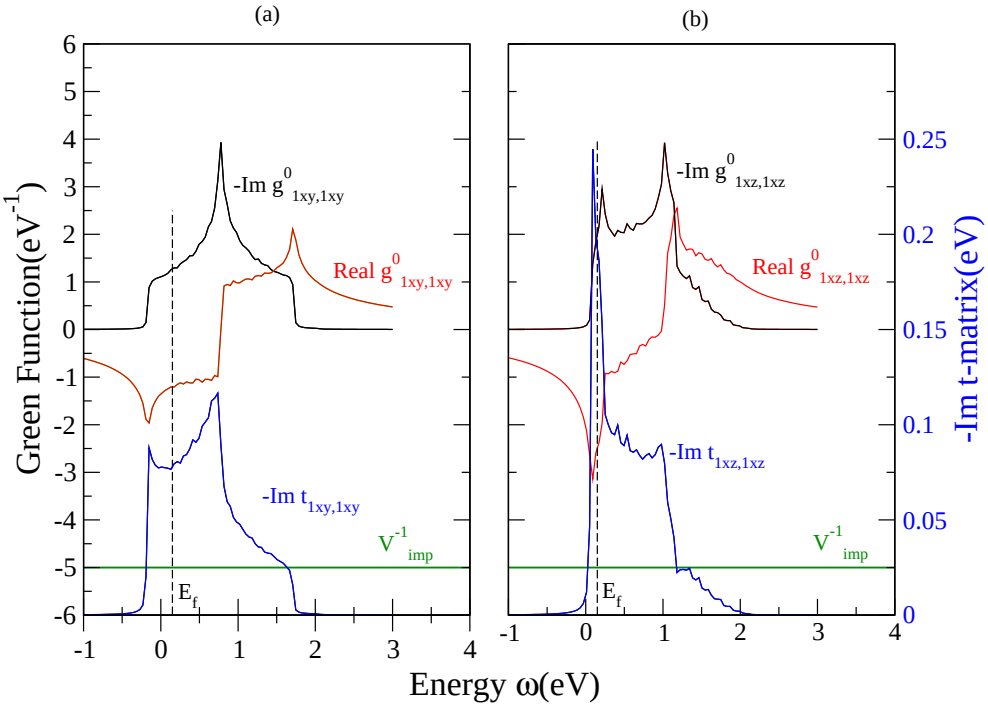

Figure 3.7: Imaginary part of the t-matrix, and imaginary and real parts of the local Green function for (a) the d_{xy} orbital, and (b) the d_{xz} and d_{yz} orbitals in layer one at impurity potential $\tilde{V}_{\rm imp} = -0.2$eV.

Figure 3.7 shows the negative of $T''_{i_z\alpha,i_z\alpha}(\omega)$, the negative of $g^{0\prime\prime}_{i_z\alpha,i_z\alpha}(\omega)$, and

$g^{0\prime}_{i_z\alpha,i_z\alpha}(\omega)$ as a function of the energy ω for the d_{xy} orbital and the $d_{xz,yz}$ orbitals in layer one at $\tilde{V}_{\rm imp} = -0.2eV$. At the Fermi energy, $g^{0\prime\prime}_{i_z\alpha,i_z\alpha}$ and $g^{0\prime}_{i_z\alpha,i_z\alpha}$ are different for the d_{xy} and $d_{xz,yz}$ orbitals. In bulk $SrTiO_3$, $g^{0}_{i_z\alpha,i_z\alpha}$ is the same for all three orbital types; however, the interface breaks this symmetry, and consequently the t-matrix is different for the d_{xy} and $d_{xz,yz}$ orbitals. This is an important reason why the xy, xz and yz bands have different scattering rates.

We note that $|\tilde{V}^{-1}_{\rm imp}| = 5{\rm eV}^{-1}$ is greater than $|g^{0\prime\prime}_{i_z\alpha,i_z\alpha}|$ and $|g^{0\prime}_{i_z\alpha,i_z\alpha}|$ at $\omega = \varepsilon_f$, so that the denominator in Eq. (3.4) is not small. This situation can be approximately understood by the Born Limit for weak scattering: when

$$|V^{-1}_{\rm imp}| \gg |g^{0\prime\prime}|, |g^{0\prime}|,$$

the imaginary part of t-matrix is, from Eq. (3.4),

$$\text{Im } T \approx g^{0\prime\prime}\tilde{V}^2_{\rm imp}.$$

This explains the structure of the scattering rate in the weak regime, where the scattering rate is nearly proportional to $\tilde{V}^2_{\rm imp}$, as shown in Fig. 3.6.

Figure 3.8 plots Eq. (3.4) at $\tilde{V}_{\rm imp} = -1.5$eV. There are two important points about Fig. 3.8. First, the imaginary part of the t-matrix is peaked outside the band edges at $\omega \approx -0.9$eV. At this value of ω, $g^{0\prime}_{i_z\alpha,i_z\alpha} = \tilde{V}^{-1}_{\rm imp}$ and $-g^{0\prime\prime}_{i_z\alpha,i_z\alpha}$ is infinitessimally small, so there is a pole in the t-matrix, as can be seen from Eq. (3.4). There is therefore a pole in $G_{u\alpha,v\beta}$ as shown in Eq. (2.61), which corresponds to bound state at $\omega \approx -0.9$eV, as shown in inset of Fig. 3.8. Second is that at the Fermi energy, $|\tilde{V}^{-1}_{\rm imp}| = 0.67{\rm eV}^{-1}$ is less than $|g^{0\prime\prime}_{i_z\alpha,i_z\alpha}|$ and $|g^{0\prime}_{i_z\alpha,i_z\alpha}|$, which corresponding to the strong scattering limit. When

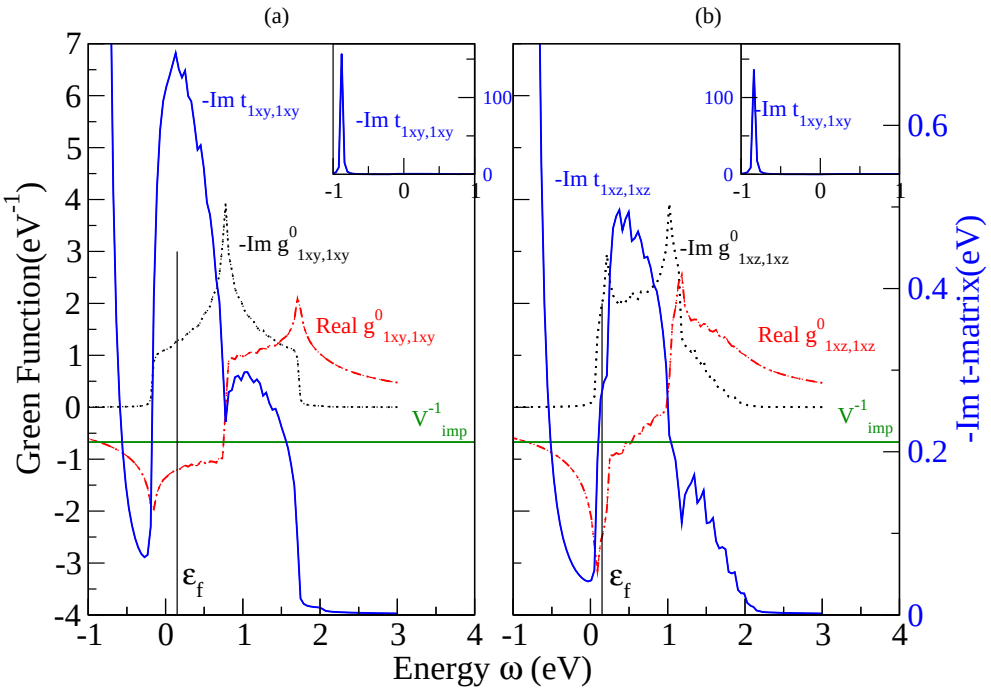

Figure 3.8: Imaginary part of the t-matrix, and imaginary and real parts of the local Green function for (a) the d_{xy} orbital, and (b) the d_{xz} and d_{yz} orbitals in layer one at impurity potential $\tilde{V}_{\rm imp} = -1.5$eV.

$$|V_{\rm imp}^{-1}| \ll |g^{0\prime\prime}|, |g^{0\prime}|,$$

the imaginary part of t-matrix is

$$\text{Im } T \approx \frac{g^{0\prime\prime}}{(g^{0\prime})^2 + (g^{0\prime\prime})^2},$$

which is independent of $\tilde{V}_{\rm imp}$. This explains the structure of the scattering rate in the strong scattering regime, where the scattering rate is nearly constant, as shown in Fig. 3.6.

To summarize, there are two scattering regimes, one in which the scattering rate strongly depends on $\tilde{V}_{\rm imp}$, and the other in which the scattering rate weakly depends on $\tilde{V}_{\rm imp}$. To understand how the fractional conductivity behaves in theses two regimes,

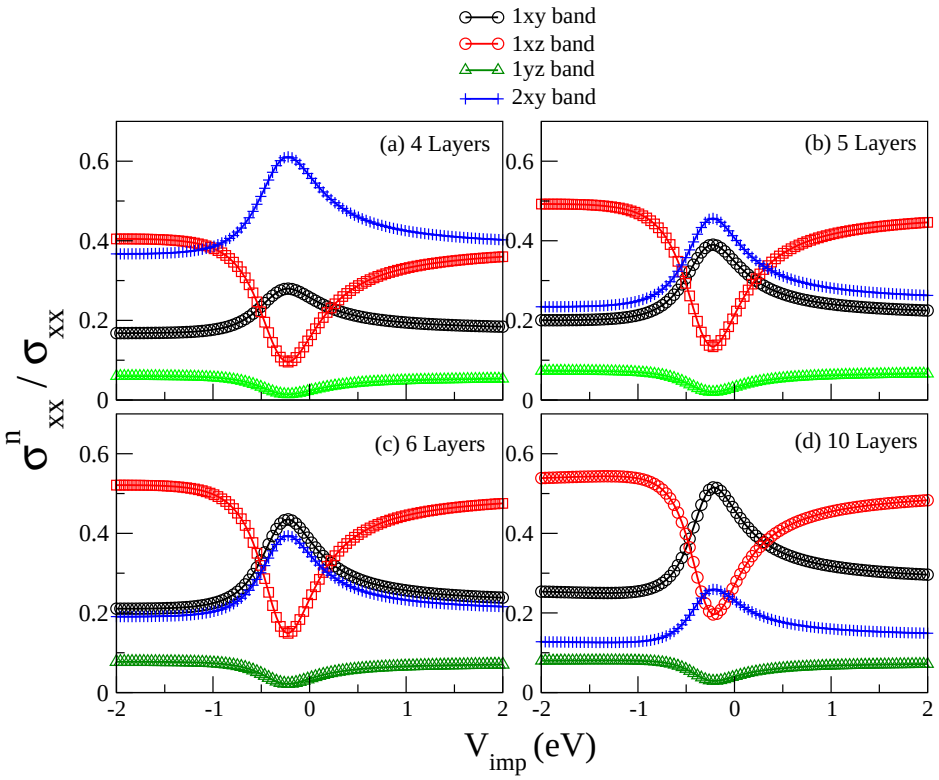

Figure 3.9: The fractional conductivity ($\frac{\sigma^n_{xx}}{\sigma_{xx}}$) for the four occupied bands ($1xy, 1xz, 1yz, 2xy$) as a function of impurity potential $\tilde{V}_{\rm imp}$ for different $SrTiO_3$ thicknesses: (a) 4 layers, (b) 5 layers, (c) 6 layers and (d) 10 layers.

we plot the fractional conductivity Eq. (3.1) for the four occupied bands as a function of $\tilde{V}_{\rm imp}$ for different film thicknesses in Fig. 3.9.

As shown in Fig. 3.9, in the weak scattering regime the fractional conductivities depend strongly on $\tilde{V}_{\rm imp}$, as with the scattering rate. When the $SrTiO_3$ film thickness is less than 5 layers, the $2xy$ band makes the biggest contribution to the 2D conductivity. When the thickness is greater than 5 layers, the $1xy$ band contribution is the biggest. The $1yz$ band makes the lowest contribution for all $SrTiO_3$ film thicknesses. For all thicknesses, the $1xy$ and $2xy$ bands have their maximum contribution, and the $1xz$ and $1yz$ bands have their minimum contribution, at $\tilde{V}_{\rm imp} = -0.2eV$.

In the strong scattering limit, the fractional conductivities weakly depend on $\tilde{V}_{\rm imp}$,

as with the scattering rate. The $1xz$ band contribution is dominant, except for the 4-layer film, where the $2xy$ band makes the biggest contribution.

To explain how the fractional conductivity of each band behaves, we look at the three parameters in Eq. (3.1) we discussed before. The large $2xy$ band contribution is because the scattering rate γ^{2xy} is two orders of magnitude smaller than γ^{1xy}, γ^{1xz} or γ^{1yz}, as shown in Fig. 3.6. The dependence of the $2xy$ band contribution on the film thickness is because the filling parameter ϵ_f^{2xy} changes slightly when the number of $SrTiO_3$ layers increases. $\varepsilon_f^{2xy} = 0.007, 0.003, 0.0029, 0.0016eV$ for the $4, 5, 6$ and 10 layers, respectively, and thus ϵ_f^{2xy} decreases with increasing film thickness. The $2xy$ contribution to the two dimensional conductivity therefore decreases. This continues as the $SrTiO_3$ layer thickness increases.

Although the $1xz$ and $1yz$ bands have similar scattering rates (Fig. 3.6) and filling (Fig. 3.3 and Table 3.2), the fractional conductivity of the $1xz$ band is 20 times bigger than the $1yz$ band due to their effective mass ratios (Table 3.2). To sum up, this discussion illustrates how the three parameters together(γ^n, ϵ_f^n and $\sqrt{\frac{m_y}{m_x}}$) influence the magnitude and structure of the contribution of each band to the 2D conductivity.

In summary, by proposing a simple model for the impurities at the $LaAlO_3/SrTiO_3$ interface, we have studied the contribution of the occupied bands to the interface conductivity. It was found that

- even though most of the charge density is confined at the first layer in the $1xy$ band, the three other occupied bands make an essential contribution to the 2D conductivity,
- the $2xy$ band makes a remarkably large contribution to the 2D conductivity, even though it has the smallest Fermi surface,
- there are two scattering regimes: the weak scattering regime in which the $1xy$

and $2xy$ band contributions are dominant, and the strong scattering regime in which the $1xz$ band has the largest fractional conductivity,

- the fractional conductivities depend on three main parameters: the filling, the effective mass ratios, and the impurity potential.

Chapter 4

Conclusion

In this thesis, we introduced a simple model to answer questions about the role of disorder in interface properties, with which we can study the contributions from occupied bands to the interface conductivity.

We solved the self-consistent Hatree equations for the interacting potential and charge density to obtain the band structure of the $SrTiO_3$ film. As a result, there were four occupied bands: the $1xy$, the $1xz$, the $1yz$ and the $2xy$ bands. By assuming that there is a low density of point-like impurities, we calculated the scattering rate for each band. Then, beginning with the semi-classical DC conductivity formula, we derived an expression for the two-dimensional conductivity at the interface. Accordingly, we calculated the relative contributions of the occupied bands to the two-dimensional conductivity, namely the fractional conductivity, as a function of impurity potential.

Our results imply that there are two scattering regimes: the weak scattering regime where the scattering rate and corresponding fractional conductivity depend significantly on the impurity potential, and the strong scattering regime where the scattering rate and the fractional conductivity are less dependent on the impurity potential. We found that there are three parameters that affect the fractional conductivity: the scattering rate, the effective mass ratios and the filling. In the weak scattering region, for a 10 layer $SrTiO_3$ film, the $1xy$ band makes the biggest contribution to the 2D conductivity because it has the biggest filling, $\epsilon_f^{1xy} = 0.319$eV. The $2xy$ band makes the second largest contribution to the 2D conductivity because it has the lowest scattering rate. The third largest contribution comes from the $1xz$ band due to both its scattering rate and filling, while the $1yz$ band has the lowest conductivity due to its small effective mass ratio, $\sqrt{\frac{m_y}{m_x}} = 0.385$. In the strong scattering region, the $1xz$ band is dominant due to its high effective mass ratio, $\sqrt{\frac{m_y}{m_x}} = 2.597$. It is noted here that we calculated the conductivity in the x-direction, and that in the y-direction, the $1xz$ and $1yz$ will exchange their contributions. The most surprising

result is that the $2xy$ band makes a significant contribution to the 2D conductivity, although it has the smallest Fermi surface area.

As we noted, the band structure of the $SrTiO_3$ film is very sensitive to any small changes. For example, a small change in the filling changes the number of occupied bands and consequently the fractional conductivity. Experimentally, the filling can be controlled by gating the interface. In future work, we will study our model for different fillings to understand how the conductivity changes. Another issue is that the dielectric constant of the $SrTiO_3$ film plays a significant role in the conductivity at the interface. In our model we fixed the dielectric constant, but in fact it is a strong function of electric field and changes from layer to layer through the $SrTiO_3$ film. Future work will include this nonlinearity. Finally, we will consider the spin-orbit interaction, which is known to be significant at the interface, and study its effect on the conductivity.

Bibliography

[1] Te Yu Chien, Jak Chakhalian, John W. Freeland and Nathan P. Guisinger, "Cross-Sectional Scanning Tunneling Microscopy Applied to Complex Oxide Interfaces," *Advanced Functional Materials* **23**, 2565-2575 (2013).

[2] J. Mannhart, D.H.A. Blank, H.Y. Hwang, A.J. Millis and J.-M. Triscone, "Two-Dimensional Electron Gases at Oxide Interfaces," *MRS BULLETIN* **33**, 1027-1030 (2008).

[3] A. Ohtomo, D. A. Muller, J. L. Grazul and H. Y. Hwang, "Artificial charge-modulationin atomic-scale perovskite titanate superlattices," *Nature* **419**, 378-380 (2002).

[4] A. Ohtomo and H. Y. Hwang, "A high-mobility electron gas at the $LaAlO_3/SrTiO_3$ heterointerface," *Nature* **427**, 423-426 (2004).

[5] C.W Schneider, S. Thiel, G. Hammerl, C. Richter and J. Mannhart, "Microlithography of electron gases formed at interfaces in oxide heterostructures," *Applied Physics Letters* **89**, 122101-122103 (2006).

[6] S. Thiel, G. Hammerl, A. Schmehl, C. W. Schneider and J. Mannhart, "Tunable QuasiTwo-Dimensional Electron Gases in Oxide Heterostructures," *Science* **313**, 1942-1945 (2006).

[7] Wolter Siemons, Gertjan Koster, Hideki Yamamoto, Walter A. Harrison, Gerald Lucovsky, Theodore H. Geballe, Dave H. A. Blank and Malcolm R. Beasley, "Origin of Charge Density at $LaAlO_3$ on $SrTiO_3$ Heterointerfaces: Possibility of Intrinsic Doping," *Phys. Rev. Lett.* **98**, 196802-196806 (2007).

[8] G. Herranz, M. ć Basleti, M. Bibes, C. Carrétéro, E. Tafra, E. Jacquet, K. Bouzehouane, C. Deranlot, A. ć Hamzi, J.-M. Broto, A. Barthélémy and A. Fert, "High Mobility in $LaAlO_3/SrTiO_3$ Heterostructures: Origin, Dimensionality, and Perspectives," *Phys. Rev. Lett.* **98**, 216803-216807 (2007).

[9] M. Sing, G. Berner, K. Goß, A. Müller, A. Ruff, A. Wetscherek, S. Thiel, J. Mannhart, S. A. Pauli, C. W. Schneider, P. R. Willmott, M. Gorgoi, F. Schäfers and R. Claessen, "Profiling the Interface Electron Gas of $LaAlO_3/SrTiO_3$ Heterostructures with Hard X-Ray Photoelectron Spectroscopy," *Phys. Rev. Lett.* **102**, 176805-176809 (2009).

[10] O. Copie, V. Garcia, C. Bödefeld, C. Carrétéro, M. Bibes, G. Herranz, E. Jacquet, J.-L. Maurice, B. Vinter, S. Fusil, K. Bouzehouane, H. Jaffrès and A. Barthélémy, "Towards Two-Dimensional Metallic Behavior at $LaAlO_3/SrTiO_3$ Interfaces," *Phys. Rev. Lett.* **102**, 216804-216808 (2009).

[11] Y. Y. Chu, Y. F. Liao, V. T. Tra, J. C. Yang, W. Z. Liu, Y.H. Chu, J. Y Lin, J. H. Huang, J. Weinen, S. Agrestini, K. D Tsuei and D. J Huang, "Distribution of electronic reconstruction at the n-type $LaAlO_3/SrTiO_3$ interface revealed by hard x-ray photoemission spectroscopy," *Applied Physics Letters* **99**, 262101 - 262104 (2011).

[12] Young Jun Chang, Luca Moreschini, Aaron Bostwick, Geoffrey A. Gaines, Yong Su Kim, Andrew L. Walter, Byron Freelon, Antonello Tebano, Karsten

Horn and Eli Rotenberg, "Layer-by-Layer Evolution of a Two-Dimensional Electron Gas Near an Oxide Interface," *Phys. Rev. Lett.* **111**, 126401-126406 (2013).

[13] J. S. Kim, S. S. A. Seo, M. F. Chisholm, R. K. Kremer, H.-U. Habermeier, B. Keimer and H. N. Lee, "Nonlinear Hall effect and multichannel conduction in $LaTiO_3/SrTiO_3$ superlattices," *Phys. Rev. B* **82**, 201407-201411 (2010).

[14] M. Radovic U. Scotti di Uccio I. Pallecchi M. Codda D. Marr C. Cantoni J. Gazquez M. Varela S. J. Pennycook P. Perna1 D. Maccariello and F. Miletto Granozio, "Conducting interfaces between band insulating oxides: the $LaGaO_3/SrTiO_3$ heterostructure," *Applied Physics Letters* **97**, 152111 (2010).

[15] A. Kalabukhov, R. Gunnarsson, T. Claeson and D. Winkler, "Electrical transport properties of polar heterointerface between $KTaO_3$ and $SrTiO_3$," *arXiv:0704.1050v1 [cond-mat.mtrl-sci]* (2007).

[16] M. Basletic, J.-L. Maurice, G. Carretero C.and Herranz, O. Copie, M. Bibes, E. Jacquet, K. Bouzehouane, S. Fusil and A. Barthelemy, "Mapping the spatial distribution of charge carriers in $LaAlO_3/SrTiO_3$ heterostructures," *Nature Materials* **7**, 621 - 625 (2008).

[17] J. Chakhalian, A. J. Millis and J. Rondinelli, "Whither the oxide interface," *NATURE MATERIALS* **11**, 9294 (2012).

[18] Naoyuki Nakagawa, Harold Y. Hwang and David A. Muller, "Why some interfaces cannot be sharp," *Nature Materials* **5**, 204 - 209 (2006).

[19] N. Reyren, S. Thiel, A. D. Caviglia, L. Fitting Kourkoutis, G. Hammerl, C. Richter, C. W. Schneider, T. Kopp, A.-S. Retschi, D. Jaccard, M. Gabay, D. A.

Muller, J.-M. Triscone1 and Mannhart J., "Superconducting Interfaces Between Insulating Oxides," *Science* **31**, 1196-1199 (2007).

[20] S Gariglio, N Reyren, A D Caviglia and J-M Triscone, "Superconductivity at the $LaAlO_3/SrTiO_3$ interface," *Journal of Physics: Condensed Matter* **21**, 164213 (2009).

[21] A. Brinkman, M. Huijben, M. Zalk van, J. Huijben, U. Zeitler, J. C. Maan, W. G. Wiel van der, G. Rijnders, D. H. A. Blank and H. Hilgenkamp, "Magnetic effects at the interface between non-magnetic oxides," *Nature Materials* **6**, 493 - 496 (2007).

[22] M. Hosoda, Y. Hikita, H. Y. Hwang and Bell C., "Transistor operation and mobility enhancement in top-gated $LaAlO_3/SrTiO_3$ heterostructures," *arXiv:1306.4351v1 [cond-mat.mtrl-sci]* (2013).

[23] Feng Bi, Mengchen Huang, Chung-Wung Bark, Sangwoo Ryu, Chang-Beom Eom, Patrick Irvin and Jeremy Levy, "Room-Temperature Electronically-Controlled Ferromagnetism at the $LaAlO_3/SrTiO_3$ Interface," *arXiv:1307.5557v1 [cond-mat.mes-hall]* (2013).

[24] W. A. Harrison, E. A. Kraut, J. R. Waldrop and R. W. Grant, "Polar heterojunction interfaces," *Phys. Rev. B* **18**, 4402–4410 (1978).

[25] Herbert Kroemer, "Polar-on-nonpolar epitaxy," *Journal of Crystal Growth* **81**, 193204 (1987).

[26] Alexey Kalabukhov, Robert Gunnarsson, Johan Börjesson, Eva Olsson, Tord Claeson and Dag Winkler, "Effect of oxygen vacancies in the $SrTiO_3$ substrate

on the electrical properties of the $LaAlO_3SrTiO_3$ interface," *Phys. Rev. B* **75**, 121404 (2007).

[27] Zhicheng Zhong, P. X. Xu and Paul J. Kelly, "Polarity-induced oxygen vacancies at $LaAlO_3SrTiO_3$ interfaces," *Phys. Rev. B* **82**, 165127 (2010).

[28] Lu Li, C. Richter, J. Mannhart and R. C. Ashoori, "Coexistence of magnetic order and two-dimensional superconductivity at $LaAlO_3/SrTiO_3$ interfaces," *Nature Physics* **7**, 762766 (2011).

[29] Julie A. Bert, Beena Kalisky, Christopher Bell, Minu Kim, Yasuyuki Hikita, Hwang Harold Y. and Kathryn A. Moler, "Direct imaging of the coexistence of ferromagnetism and superconductivity at the $LaAlO_3/SrTiO_3$ interface," *Nature Physics* **7**, 767771 (2011).

[30] J.-S. Lee, Y. W. Xie, H. K. Sato, C. Bell, Y. Hikita, Hwang H. Y. and C.-C. Kao, "Titanium d_{xy} ferromagnetism at the $LaAlO_3/SrTiO_3$ interface," *Nature Materials* **12**, 703706 (2013).

[31] Z. Q. Liu, C. J. Li, W. M. Lü, X. H. Huang, Z. Huang, S. W. Zeng, X. P. Qiu, L. S. Huang, A. Annadi, J. S. Chen, J. M. D. Coey, T. Venkatesan and Ariando, "Origin of the Two-Dimensional Electron Gas at $LaAlO_3/SrTiO_3$ Interfaces: The Role of Oxygen Vacancies and Electronic Reconstruction," *Phys. Rev. X* **3**, 021010 (2013).

[32] P. R. Willmott, S. A. Pauli, R. Herger, C. M. Schlepütz, D. Martoccia, B. D. Patterson, B. Delley, R. Clarke, D. Kumah, C. Cionca and Y. Yacoby, "Structural Basis for the Conducting Interface between $LaAlO_3$ and $SrTiO_3$," *Phys. Rev. Lett.* **99**, 155502 (2007).

[33] Y. Segal, J. H. Ngai, J. W. Reiner, F. J. Walker and C. H. Ahn, "X-ray photoemission studies of the metal-insulator transition in $LaAlO_3/SrTiO_3$ structures grown by molecular beam epitaxy," *Phys. Rev. B* **80**, 241107 (2009).

[34] Scott A. Chambers, "Understanding the mechanism of conductivity at the $LaAlO_3/SrTiO_3$ (001) interface," *Surface Science* **605**, 1133-1140 (2011).

[35] L. Qiao, T.C. Droubay, T.C. Kaspar, P.V. Sushko and S.A. Chambers, "Cation mixing, band offsets and electric fields at $LaAlO_3/SrTiO_3$ (001) heterojunctions with variable La:Al atom ratio," *Surface Science* **605**, 1381-1387 (2011).

[36] C. Cantoni, J. Gazquez, F. Miletto Granozio, Miletto Granozio, M. P. Miletto Granozio, M. Varela, A. R. Lupini, S. J. Pennycook, C. Aruta, U. S. Uccio di, P. Perna and D. Maccariello, "Millimetre wave spectroscopy of high Rydberg states," *Advanced Materials* **24**, 39523957 (2012).

[37] V. Vonk, J. Huijben, D. Kukuruznyak, A. Stierle, H. Hilgenkamp, A. Brinkman and S. Harkema, "Polar-discontinuity-retaining *A*-site intermixing and vacancies at $SrTiO_3/LaAlO_3$ interfaces," *Phys. Rev. B* **85**, 045401 (2012).

[38] A. S. Kalabukhov, Yu. A. Boikov, I. T. Serenkov, V. I. Sakharov, V. N. Popok, R. Gunnarsson, J. Börjesson, N. Ljustina, E. Olsson, D. Winkler and T. Claeson, "Cationic Disorder and Phase Segregation in $LaAlO_3/SrTiO_3$ Heterointerfaces Evidenced by Medium-Energy Ion Spectroscopy," *Phys. Rev. Lett.* **103**, 146101 (2009).

[39] Mark Huijben, Alexander Brinkman, Gertjan Koster, Guus Rijnders, Hans Hilgenkamp and Dave H. A. Blank, "Remarks concerning moleculal interaction and their influence on the polarisability," *Advanced Materials* **21**, 16651677 (2009).

[40] Yun Li, Sutassana Na Phattalung, Sukit Limpijumnong, Jiyeon Kim and Jaejun Yu, "Formation of oxygen vacancies and charge carriers induced in the n-type interface of a $LaAlO_3$ overlayer on $SrTiO_3(001)$," *Phys. Rev. B* **84**, 245307 (2011).

[41] N. C. Bristowe, P. B. Littlewood and Emilio Artacho, "Surface defects and conduction in polar oxide heterostructures," *Phys. Rev. B* **83**, 205405 (2011).

[42] C. Cen, S. Thiel, G. Hammerl, C. W. Schneider, K. E. Andersen, C. S. Hellberg, J. Mannhart and J. Levy, "Nanoscale control of an interfacial metalinsulator transition at room temperature," *Nature Materials* **7**, 298-302 (2008).

[43] M. Salluzzo, S. Gariglio, D. Stornaiuolo, V. Sessi, S. Rusponi, C. Piamonteze, G. M. De Luca, M. Minola, D. Marr, A. Gadaleta, H. Brune, F. Nolting, N. B. Brookes and G. Ghiringhelli, "Origin of interface magnetism in BiMnO3/SrTiO3 and LaAlO3/SrTiO3 heterostructures," *arXiv:1305.2226v2 [cond-mat.str-el]* (2013).

[44] J. Park, B.-G. Cho, K. D. Kim, J. Koo, H. Jang, K.-T. Ko, J.-H. Park, K.-B. Lee, J.-Y. Kim, D. R. Lee, C. A. Burns, S. S. A. Seo and H. N. Lee, "Oxygen-Vacancy-Induced Orbital Reconstruction of Ti Ions at the Interface of $LaAlO_3/SrTiO_3$ Heterostructures: A Resonant Soft-X-Ray Scattering Study," *Phys. Rev. Lett.* **110**, 017401 (2013).

[45] L. F. Mattheiss, "Energy Bands for $KNiF_3$, $SrTiO_3$, $KMoO_3$, and $KTaO_3$," *Phys. Rev. B* **6**, 4718-4740 (1972).

[46] S James Allen, Bharat Jalan, SungBin Lee, Daniel G. Ouellette, Guru Khalsa, Jan Jaroszynski, Susanne Stemmer and Allan H. MacDonald, "Shubnikov-de Haas effect in low electron density $SrTiO_3$: Conduction band edge of $SrTiO_3$ redux," *arXiv:1304.7737v1 [cond-mat.str-el]* (2013).

[47] Rossitza Pentcheva and Warren E Pickett, "Electronic phenomena at complex oxide interfaces: insights from first principles," *Journal of Physics: Condensed Matter* **22**, 043001 (2010).

[48] Hanghui Chen, Alexie Kolpak and Sohrab Ismail-Beigi, "First-principles study of electronic reconstructions of $LaAlO_3/SrTiO_3$ heterointerfaces and their variants," *Phys. Rev. B* **82**, 085430 (2010).

[49] Guru Khalsa and A. H. MacDonald, "Theory of the $SrTiO_3$ surface state two-dimensional electron gas," *Phys. Rev. B* **86**, 125121 (2012).

[50] Zhicheng Zhong, Philipp Wissgott, Karsten Held and Giorgio Sangiovanni, "Microscopic understanding of the orbital splitting and its tuning at oxide interfaces," *EPL(Europhysics Letters)* **99**, 37011 (2012).

[51] Zhicheng Zhong, Qinfang Zhang and Karsten Held, "Quantum confinement in perovskite oxide heterostructures: Tight binding instead of a nearly free electron picture," *Phys. Rev. B* **88**, 125401 (2013).

[52] Zhicheng Zhong, Anna Tóth and Karsten Held, "Theory of spin-orbit coupling at $LaAlO_3/SrTiO_3$ interfaces and $SrTiO_3$ surfaces," *Phys. Rev. B* **87**, 161102 (2013).

[53] Satoshi Okamoto, Andrew J. Millis and Nicola A. Spaldin, "Lattice Relaxation in Oxide Heterostructures: $LaTiO_3/SrTiO_3$ Superlattices," *Phys. Rev. Lett.* **97**, 056802 (2006).

[54] E. N. Economou, *Green's Functions in Quantum Physics*, (Springer Berlin Heidelberg, Springer-Verlag Berlin Heidelberg, 3rd edition, 2006, chapter 6).

[55] E. N. Economou, *Green's Functions in Quantum Physics*, (Springer Berlin Heidelberg, Springer-Verlag Berlin Heidelberg, 3rd edition, 2006, section 7.2.2).

[56] Henrik Bruus and Karsten Flensberg, *Many-Body Quantum Theory in Condensed Matter Physics: An Introductions*, (Oxford University Press, section 11.5.4).

[57] Neil W. Ashcroft and N. David Mermin, *Solid State Physics*, (Brooks Cole, chapter 13).

[58] Zoran S. ć Popovi, Sashi Satpathy and Richard M. Martin, "Origin of the Two-Dimensional Electron Gas Carrier Density at the $LaAlO_3$ on $SrTiO_3$ Interface," *Phys. Rev. Lett.* **101**, 256801 (2008).

[59] M. Salluzzo, J. C. Cezar, N. B. Brookes, V. Bisogni, G. M. De Luca, C. Richter, S. Thiel, J. Mannhart, M. Huijben, A. Brinkman, G. Rijnders and G. Ghiringhelli, "Orbital Reconstruction and the Two-Dimensional Electron Gas at the $LaAlO_3/SrTiO_3$ Interface," *Phys. Rev. Lett.* **102**, 166804 (2009).

[60] Jichao C. Li, Juan Ignacio Beltrán and M. Carmen Muñoz, "Multiorbital structure of the two-dimensional electron gas in $\mathbf{LaAlO_3}/SrTiO_3$ heterostructures: The formation of a $\mathbf{d_{xy}}$ ferromagnetic sheet," *Phys. Rev. B* **87**, 075411 (2013).

Appendix

A. Derivation of Coulomb Potential $\phi^{\mathrm{C}}_{i_z\alpha}$

The Coulomb potential in the $SrTiO_3$ film is

$$\phi^{\mathrm{C}}_{i\alpha} = \sum_{j\beta\sigma} V_{i\alpha,j\beta} n_{j\beta\sigma}, \tag{1}$$

or

$$\phi_{i\alpha} = \sum_{j\beta\sigma} V(i_x - j_x, i_y - j_y, i_z - j_z) n_{j\beta\sigma}. \tag{2}$$

We assume that each layer has a homogeneous charge distribution; so that the potential in the x-y plane is constant. Hence, the Coulomb potential is

$$\phi_{i\alpha} = \sum_{\beta\sigma} \tilde{V}(i_z - j_z) n_{j_z\beta\sigma}, \tag{3}$$

where

$$\tilde{V}(i_z - j_z) = \sum_{j_x j_y} V(j_x, j_y, i_z - j_z). \tag{4}$$

Explicitly,

$$\tilde{V}(i_z - j_z) = \sum_{\vec{\rho}\neq 0} \frac{e^2}{4\pi\epsilon_0\kappa} \frac{1}{\sqrt{\rho^2 + (i_z - j_z)^2 a^2}}, \tag{5}$$

where ρ is a two-dimensional vector in the x and y-direction. To calculate $\tilde{V}(i_z - j_z)$, we imagine the layer is a disk of radius R, so that

$$\tilde{V}(i_z - j_z) = \int_0^R \rho d\rho \int_0^{2\pi} d\theta \frac{e^2}{4\pi\epsilon_0\kappa} \frac{1}{\sqrt{\rho^2 + (i_z - j_z)^2 a^2}}, \tag{6}$$

$$\tilde{V}(i_z - j_z) = \frac{2\pi e^2}{4\pi\epsilon_0\kappa} \sqrt{\rho^2 + (i_z - j_z)^2 a^2}\Big|_0^R, \tag{7}$$

$$\tilde{V}(i_z - j_z) = \frac{e^2}{2\epsilon_0\kappa}(R - |i_z - j_z|a). \tag{8}$$

Since the potential,

$$\frac{e^2R}{2\epsilon_0\kappa},$$

is constant, it can be dropped from $\tilde{V}$, and we let

$$\tilde{V}(i_z - j_z) = \frac{-e^2}{2\epsilon_0 k}|i_z - j_z|a. \tag{9}$$

Therefore, the Coulomb potential is

$$\phi_{i_z\alpha} = \frac{-e^2a}{2\epsilon_0 k}\sum_{j_z}\sum_{\beta\sigma}|i_z - j_z|n_{j_z\beta\sigma}. \tag{10}$$

For computational convenience, we redefine $\phi_{i_z\alpha}$ as

$$\phi_{i_z\alpha} \to \phi_{i_z\alpha} - \phi_{i_z=0,\alpha}.$$

Finally, the Coulomb potential is

$$\phi_{i_z\alpha} = \frac{-e^2a}{2\epsilon_0 k}\sum_{j_z}\sum_{\beta}(|i_z - j_z| - j_z)n_{j_z\beta\sigma}. \tag{11}$$

Appendix

B. Derivation of Charge Density $n_{j_z\beta\sigma}$

The charge density for a certain layer j, orbital type β, and spin σ can be expressed as,

$$n_{j\beta\sigma} = \langle c^{\dagger}_{j\beta\sigma} c_{j\beta\sigma} \rangle, \tag{12}$$

then we perform the Fourier transform in the x and y-direction

$$c_{j\beta\sigma} = \frac{1}{\sqrt{N}} \sum_{k_x k_y} e^{i\vec{k}\cdot\vec{r}_{j_x j_y}} c_{j_z\beta\sigma\vec{k}}, \tag{13}$$

then

$$\therefore n_{j\beta\sigma} = \frac{1}{N} \sum_{\vec{k},\vec{k}'} e^{i(\vec{k}-\vec{k}')\cdot\vec{r}_{j_x j_y}} \langle c^{\dagger}_{j_z\beta\sigma\vec{k}'} c_{j_z\beta\sigma\vec{k}} \rangle. \tag{14}$$

Then, we transform to a basis in which the Hamiltonian $\hat{H}_{HF}$ is diagonal. Since $\psi_{i_z\alpha\sigma,n}(\vec{k})$ diagonalizes $\mathbf{H}(\vec{k})$, then

$$H_{i_z\alpha\sigma,j_z\beta\sigma}(\vec{k}) = \sum_n \psi_{i_z\alpha\sigma,n}(\vec{k}) E_n(\vec{k}) \psi^*_{j_z\beta\sigma,n}(\vec{k}). \tag{15}$$

Define

$$a_{n\vec{k}} = \sum_{j_z\beta\sigma} \psi^*_{j_z\beta\sigma,n}(\vec{k}) c_{j_z\beta\sigma}, \tag{16}$$

then

$$\hat{H}_{HF} = \sum_{n\vec{k}} E_n(\vec{k}) a^{\dagger}_{n\vec{k}} a_{n\vec{k}}. \tag{17}$$

Substituting Eq. (16) into Eq. (14), we obtain

$$n_{j_z\beta\sigma} = \frac{1}{N} \sum_{\vec{k}\vec{k}'} e^{i(\vec{k}-\vec{k}')\cdot\vec{r}_{j_x j_y}} \sum_{nm} \psi^*_{j_z\beta\sigma,n} \langle a^{\dagger}_{n\vec{k}} a_{m\vec{k}'} \rangle \psi_{j_z\beta\sigma,m}. \tag{18}$$

Since the expectation values $\langle a^{\dagger}_{n\vec{k}} a_{m\vec{k}'} \rangle$ are with respect to eigenstates of $\hat{H}_{HF}$,

then

$$\langle a^{\dagger}_{n\vec{k}} a_{m\vec{k}'} \rangle = \delta_{n,m}\delta_{\vec{k}\vec{k}'} f(\varepsilon_{n\vec{k}}), \tag{19}$$

equals zero unless $m = n$ and $\vec{k} = \vec{k}'$.

Finally, the charge density $n_{j_z\beta\sigma}$ is

$$n_{j_z\beta\sigma} = \frac{1}{N} \sum_{\vec{k}} \sum_{n} |\psi_{j_z\beta\sigma,n}(\vec{k})|^2 f(\varepsilon_{n\vec{k}}). \tag{20}$$